Pattern Dynamics in the Electrohydrodynamics of Nematic Liquid Crystals
—— *Defect Patterns, Transition to Turbulence and Magnetic Field Effects*——

Shoichi KAI and Walter ZIMMERMANN*

Department of Electrical Engineering, Kyushu Institute of Technology, Kitakyushu 804
**IFF Theorie III, Forschungszentrum Juelich KFA, D-5170 Juelich*
Fed. Rep. of Germany

Various patterns in the electrohydrodynamic convection of planarly aligned nematic liquid crystals are investigated. We give experimental and theoretical results on the onset of convection in the conduction regime and the dielectric regime as well. The transition to the fluctuating Williams domain (FWD) immediately above the onset of convection in the conduction regime is characterized in detail. At this secondary threshold the straight rolls become unstable and defects appear. During the temporal development of the FWD, defects are continuously created and annihilated, and the defect density behaves rather stochastical in time. At even higher values of the applied voltage we investigate the transition between the two turbulent states DSM1 and DSM2 which has some analogy with TI-TII transition in superfluid HeII. DSM2 turbulence can be characterized by disclination and therefore called disclination turbulence. We show that this transition is local via nucleation and that the main difference between both states is the vanishing disclination density in the DSM1 state and its finite value in the DSM2. In the high frequency regime we analyse the secondary transition to chevrons and the defect dynamics in this pattern as a periodic defect structure. Furthermore, the influence of a superimposingly applied magnetic field on these patterns is considered.

§ 1. Introduction

A dissipative system driven far from equilibrium by increasing values of an external control-parameter may undergo a sequence of transitions (bifurcations).[1)~13)] Often the equilibrium state is spatially and temporally uniform and the subsequent bifurcations lead to states of decreasing symmetry. These new states are in general theoretically described by highly nonlinear equations. During the last decade great progress has been achieved in understanding of the formation and dynamics of many patterns in various systems beyond each such a bifurcation point by a huge amount of experimental measurements and theoretical activities (in particular, analytical as well as large numerical computations). Several of these insights also have importance on the qualitative level far beyond well-defined physical systems, like biology and economy. Rayleigh-Bénard (R-B) convection and Taylor vortex flow,[1)~4)] which are well known already about a century, are two of these well-defined physical systems where a huge of experimental and theoretical investigations have been done and which were a source of the mentioned insights. Both examples provided the

Downloaded from https://academic.oup.com/ptps/article/doi/10.1143/PTPS.99.458/1882039 by guest on 21 August 2022

motivation for many nonlinear theories and also a lot of theoretical considerations were tested in these systems.

The electrohydrodynamic (EHD) instability of nematic liquid crystals (NLCs) was discovered more recently——about three decades ago[5] and intensively investigated in a first period in the early '70th. This activity was mainly motivated by the perspective of potential applicability of EHD convection in commercial displays, whereas the recently observable renaissance of investigations of EHD convection is mainly induced by the increasing general interest in the formation and dynamics of patterns in nonequilibrium systems. Especially the observed Hopf bifurcation to supercritical travelling waves[7)~9),14)~17)] and defect chaos[9)~12),14)~17)] in EHD convection are quite fashionable subjects to be understood, whereas the occurrence in this systems has several advantages in comparison with other systems. Now EHD convection becomes more and more a paradigmatic example for pattern formation like R-B convection and Taylor vortex flow.

NLCs consist of long organic molecules which show in some temperature range (often room temperature) a nematic phase. In the nematic phase the molecules orient in the mean along a main direction, described by the director $\boldsymbol{n}$ ($\boldsymbol{n}=-\boldsymbol{n}$). However the position-order of the molecules is random as in simple fluids (for more details see e.g., Ref. 6)).

The geometry of most experiments on EHD convection in NLCs is in some respect similar to the geometry of the well-known R-B convection. A nematic material is brought between two glass plates which are parallel and usually at a distance of 5-200 μm (layer thickness: d). The horizontal extension is mainly some centimeters and the inside of the glass plates are evaporated by some conducting material like SnO_2. By an appropriate surface treatment the molecules of NLC at the glass surface can be fixed in a defined orientation. We here consider always the situation where the mean orientation, the director (planar orientation), aligns parallel to the surface along one fixed direction which we call the x-direction. Then due to elastic forces the same orientation is uniformly obtained in the whole sample, if no voltage is applied. When a temporally alternating voltage is applied across a thin layer of nematic liquid crystal with negative ε_a and ionic conductivity, an instability occurs at a certain voltage V_c which, under ideal conditions, leads to a periodic pattern of convection rolls connected with periodic distortions of the director. This is originally called the electrohydrodynamic instability.[6]

In EHD convection, temperature difference between the bottom and the top of a fluid layer in R-B convection is replaced by the square of an electric potential V (voltage).[14] Similarly the frequency f of an applied voltage corresponds to the inverse of Prandtl number $Pr(=\tau_\kappa/\tau_\nu)$ through characteristic time τ_κ for thermal mode replaced by one for the space charge mode and a characteristic time τ_ν of viscous mode by one of the elastic deformation mode.[14),15)] The competition of these two modes leads to a critical frequence f_c and shows two different regimes for pattern formations, i.e., "conduction" and "dielectric" regimes. In accordance with these analogues, a very similar phase diagram for fluid patterns to that in R-B convection can be obtained as previously reported, where a typical route to turbulence in EHD is as follows.[14]

Downloaded from https://academic.oup.com/ptps/article/doi/10.1143/PTPS.99.458/1882039 by guest on 21 August 2022

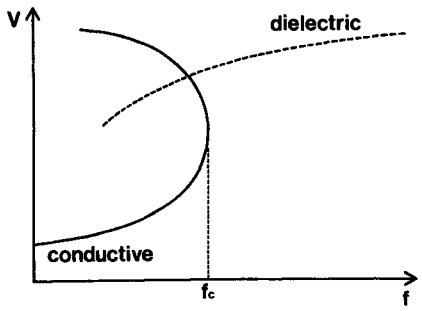

Fig. 1.1. Stability diagram for EHD convection in frequency-voltage plane. The solid and dot lines show the thresholds above which convections take place.

In the "conduction" regime below f_c above the threshold one has convection rolls (Williams domain: WD) which orient normal or oblique to the undistorted director orientation. Here f_c is a critical frequency separating the "dielectric" and the "conductive" regimes in EHD (see Fig. 1.1).[6] At a higher voltage one finds a secondary bifurcation to the fluctuating WD (FWD). In that regime one observes defect chaos. Defects are continuously created and annihilated, the defect number in a unit area fluctuates and never becomes stationary.[12),17)] Increasing the voltage further one observes a transition to Grid-Pattern (GP).[16)] GP can be stationary or oscillatory. If one has a strong dynamics of the defect often the Gird-Pattern is oscillatory.[17)] At even higher voltages one observes a transition to a turbulent state. The turbulent state in EHD convection is called the dynamic scattering mode (DSM) and this mode which occurs above the GP, we call DSM1. Increasing the voltage further a transition from DSM1 to another dynamic scattering mode (DSM2) happens (see § 4 in detail). Increasing the voltage at higher frequencies but still below f_c, at threshold often convection sets in via travelling waves. In the "dielectric" regime (above f_c) immediately above threshold one observes often a short wavelength (several μm) periodic stripe pattern, where the wavelength is rather independent of the thickness. At a second threshold one observes often a transition to a quasi-periodic pattern, the so-called chevrons. Sometimes chevrons are already visible immediately at the first threshold see below (see § 5). About more different patterns in EHD convection we refer to Refs. 15)~19).

Besides a different stability diagram the EHD convection in nematics has a number of properties which distinguish it from others much more investigated systems like R-B convection and Taylor vortex flow. In EHD, due to the small thickness of the convection layer the relaxation times are much shorter and one can easily produce specimens with large aspect ratios Γ (=ratio of the lateral dimension to the thickness) in one or two directions. In addition to the amplitude of the applied voltage one has the frequency as an easily accessible external-control-parameter. This, together with the facts that the material couples strongly to an additionally applied magnetic field and that a vast variety of nematics with different material constants are available, provides for very rich scenarios. However only with one material (MBBA) most of the experiments have been done and it is also the only material with a nematic phase at room temperature where all material constants are known. As a result of the planar orientation of the director at the upper and the lower plate there is an axial anisotropy, so that the patterns (WD, GP, etc.) orient with respect to the preferred axis (no rotational invariance in the plane of the layer). From symmetry reasons at the first threshold only rolls or possibly a rectangular structure is expected to appear near threshold. The existence and stability of roll solutions above threshold should

Downloaded from https://academic.oup.com/ptps/article/doi/10.1143/PTPS.99.458/1882039 by guest on 21 August 2022

in this system be considered in terms of two-dimensional wavevector areas[20)~22)] instead of the wavenumber bands adequate for isotropic systems like R-B convection.

The characteristic features for pattern formation processes of WD have been already discussed and three different stages are found during pattern selection processes.[15)] In the early stage, a uniquely selected linear mode (the most rapidly growing mode) grows initially and then nonlinear modes become more stable in the intermediate stage.[15)] In the final stage, as a result of the competitive growth among nonlinear modes, defects are formed and a final pattern selection is successful through defect motions, i.e., gliding and climbing.[15)] The spontaneously oscillatory gliding and climbing of a single defect are also reported.[15),19),23)] Such an oscillatory behavior of a single defect has been never observed in isotropic R-B systems and the amplitude equations currently obtained in EHD for anisotropic fluid cannot succeed to describe it. Therefore we have suggested that the detailed investigation on a single defect motion is important for determining a type of true amplitude equations for EHD.[19)]

After the first bifurcation to stationary convection, often at a second threshold slightly above V_c, FWD occur.[23),24)] This convection is mainly characterized by finite defect density as well as continuous nucleation and annihilation of defects and complex defect dynamics has been characterized in some extents.[19)] However the origin is not well understood yet.[15)] Recently great attention is focussed on this state; that is, a possibility of theoretical description for it, definition of defect chaos, nature of bifurcation and the mechanism of creation of defects.[10),11)] In § 3 of this article we will discuss the further progress.

Fully developed turbulence occurs at sufficiently strong external fields applied to fluid systems.[13)] It attracts great interest already more than a century.[1)] Especially in small aspect ratio systems during the last decade there has been considerable progress in understanding essential features in the framework of nonlinear dynamical systems.[4)] In large aspect ratio systems the understanding of turbulence is less advanced. Different routes to turbulence have been found in both cases, however in simple fluids on such a route most of the bifurcations are spatially homogeneous. A transition to turbulence in EHD shows quite new aspect. Section 4 is devoted to the detail on this spatially inhomogeneous turbulence-turbulence transition. We find here similarity with classical crystal growth kinetics and with the turbulence-turbulence (TI-TII) transition in HeII,[25)~27)] where the analogy between director field in EHD and superfluid velocity field in HeII will be pointed out.

In EHD however even the onset of convection is still not fully understood. In particular, it is already known more than a decade that travelling waves (a Hopf bifurcation) occur at the first threshold, mainly in the conduction regime near the cutoff frequency f_c.[17),24)] Recently more detailed measurements have confirmed these observations.[9)] However the mechanism which leads to travelling waves at the onset of convection is still open. The experimental groups use different sample preparation and obtain also different frequency ranges for the occurrence of travelling waves. Theoretically only the threshold problem was solved within various approximations. Recently this problem has been solved in the conduction regime by neglecting the flexoelectric effect[21)] and later without any further assumption, by solving the accepted hydrodynamic equations for EHD convection in the whole frequency range

Downloaded from https://academic.oup.com/ptps/article/doi/10.1143/PTPS.99.458/1882039 by guest on 21 August 2022

for the first time rigorously.[16] However a Hopf-bifurcation was not found for a reasonable set of parameters. In § 5 we discuss the results on the stationary bifurcation by solving the full linear set of equations and their consequences, especially in the dielectric regime. The chevron pattern[28] observed in the dielectric regime can be regarded in a sense as a kind of periodic defect orientation[19] due to modurated potential for defects. A co-dimension-two(CDT)-bifurcation at another critical frequency f_c^* higher than f_c is observed experimentally.[29] This behavior however is not observed by currently available theories.

Nematic liquid crystals can respond not only to an electric field E but also to a magnetic field H.[6] The director of NLC aligns parallel to the direction of H since $\chi_a>0$, contrary to the orientation induced by an electric field. Namely a roll aligns with the direction perpendicular to that of H under strong enough H. Here $\chi_a=\chi_{/\!/}-\chi_\perp$ is the anisotropic magnetic susceptibility of NLCs, and $\chi_{/\!/}$ and $\chi_\perp$ are the magnetic susceptibilities parallel and perpendicular to the director. Here two directions of H are distinguished: $H_{/\!/}$ and $H_\perp$, indicating the magnetic fields parallel and perpendicular to E, respectively. Most of the presented studies are performed for $H_\perp$, where the direction of H is only changed in a plane and maintained perpendicular to E. This leads to additional variety of phenomena in EHD,[19] a part of which will be shown in § 6. We already reported that the magnetic field suppresses the defect chaos and stabilizes the system, that is, the threshold of the applied electric field for the onset of EHD shifts up when the magnetic field increases.[19] The magnetic field can also change the direction of the roll axis into that perpendicular to the external field and leads more easily to zig-zag and oblique patterns.[19] Further details on magnetic field effects will be given in this section, i.e., particularly thickness dependence of Freedericksz transition superimposing EHD.[30]

In the present paper, since the experimental techniques and manners have been already described,[15] we concentrate only to describe our results together with recent theories for EHD.[20~22]

§ 2. Theoretical consideration for onset of convection and threshold behavior in EHD

The basic mechanism for the onset of convection has been already understood and described for an applied dc-voltage by Helfrich.[31] By the Orsay group[32] this was extended to an ac-voltage and it was recognized within the one-dimensional approximation that there are two different frequency-regimes, the low frequency conduction and the high frequency dielectric regime at the onset of convection (see for example Fig. 1.1). In the conduction regime convection rolls have a wavelength of the order of the thickness of the fluid layer and the director is mainly stationary in time with small modulations, whereas in the dielectric regime the director is mainly oscillating with the external frequency and the stationary part is smaller. The wavelength of the periodic pattern in the dielectric regime is much smaller than the layer thickness and is for large ranges independent of the thickness and the conductivity. This could be already roughly understood in the framework of the one-dimensional model (ODM) calculation.[5),6]

Originally it was assumed that the periodic pattern occurs at threshold always

Downloaded from https://academic.oup.com/ptps/article/doi/10.1143/PTPS.99.458/1882039 by guest on 21 August 2022

with the roll axis normal to the undistorted director orientation (normal rolls), which was often experimentally confirmed. However more recently Hilsum and Saunders[33] observed that there is a secondary transition to an oblique roll convection structure. Later it was also observed that there can be oblique rolls already at the onset of convection, which is also understood in an approximate three-dimensional calculation.[20] The transition to oblique rolls at the threshold could be understood in the framework of ODM as originally done by the Orsay group, by taking the flexoelectric effect into account.[34] In the conduction regime the onset of convection via travelling waves has been also observed some time ago.[17),24] But unfortunately theoretically the occurrence of a Hopf bifurcation could not be predicted, even by a rigorous solution of the full linearized-hydrodynamic-equations without further assumptions.[35] However the rigorous solution of the linear equation by including the flexoelectric effect provides a more detailed picture for the stationary bifurcation and other interesting and important properties, which will be described below.

The basic equation for EHD convection considered here is provided by the standard hydrodynamic description of NLCs[21] and for the same equations including the flexoelectric effect.[35] They consist of momentum balance (Navier-Stokes equation) together with incompressibility $\boldsymbol{\nabla}\cdot\boldsymbol{v}=0$, which determine the velocity field $\boldsymbol{v}$, and the balance of torque which gives the director $\boldsymbol{n}$. Moreover, there are electric field equations (Maxwell and charge conservation equations) in the quasi-static approximation. The complete electric field is the superposition of induced and an applied part: $\boldsymbol{E}=-\boldsymbol{\nabla}\phi+(V(t)/d)\hat{z}$ and for the director we use the representation $\boldsymbol{n}=(\cos\Theta\cos\Psi,\ \cos\Theta\sin\Psi,\ \sin\Theta)$. All these equations are coupled and provide a highly nonlinear set of equations for the three velocity components, two angles for the director and the induced electric potential ϕ.

The threshold for EHD is calculated by assuming that all quantities deviate only very slightly from their values in the basic unstructured-state, which is characterized by $\boldsymbol{v}=0$, $\boldsymbol{n}=(1,0,0)$ and vanishing induced potential $\phi=0$ (which is equivalent to vanishing charge density). We then write $\boldsymbol{n}=(1,\Psi,\Theta)$ and linearize the equations in the small deviations.[20)~22),35]

The resulting set of linear partial differential equations (PDE) for $\boldsymbol{u}=\{\phi,\Theta,\Psi,\boldsymbol{v}\}$ is translational invariant with respect to x and y and therefore the solutions are harmonic and may be chosen proportional to $\sin(qx+py)$ and $\cos(qx+py)$; wavevector $(q,p)=(2\pi/\lambda_{x,y})$ where $\lambda_{x,y}$ are the wavelength of the convective structure in the x- and y-directions. For the voltage applied between the plates we only assume that it has the periodicity T in time: $V(t)=\bar{V}\cdot f(t)$, with $f(t)=f(t+T)$. The set of linear equations has then the formal structure,

$$\underset{\sim}{M}(t,\partial_z)\partial_t\boldsymbol{u}(z,t)=\underset{\sim}{L}(t,\partial_z)\boldsymbol{u}(z,t)\,, \tag{2·1}$$

where the 6×6 matrices $\underset{\sim}{M}$ and $\underset{\sim}{L}$ contain derivatives with respect to z and depend on q, p and $V(t)$ and they have the periodicity T in time. Rigid planar anchoring of the director and ideal conducting electrodes——which presumably come near to the reality——are assumed. Therefore we have the boundary conditions

Downloaded from https://academic.oup.com/ptps/article/doi/10.1143/PTPS.99.458/1882039 by guest on 21 August 2022

$$\boldsymbol{u}=0 \quad \text{and} \quad z=\pm d/2 \tag{2·2}$$

(from $\nabla\cdot\boldsymbol{v}=0$ we also have $\partial_z v_z=0$ at $z=\pm d/2$).

For periodic driving voltage $V(t)$ the linear modes are expected to be of the form

$$\boldsymbol{u}(z,t)=\boldsymbol{u}'(z,t)\exp(\sigma t)\,, \quad \sigma=\sigma_r+i\sigma_i\,, \tag{2·3}$$

where, according to the Floquet theorem[36] $\boldsymbol{u}'$ is periodic in t with period T. For the numerical solution of Eq. (2·1) we use for each component $\boldsymbol{u}'_k$ an expansion into a complete set of z-dependent function:[20)~22)]

$$\boldsymbol{u}'_k(z,t)=\sum_{j=1}^{N}\boldsymbol{w}_{kj}(t)\Lambda_{k,j}(z)\,. \tag{2·3a}$$

Equation (2·1) is then transformed into a set of ordinary differential equations (ODE) for $\boldsymbol{W}=(\boldsymbol{w}_1,\cdots,\boldsymbol{w}_N)$ $(\boldsymbol{w}_k=(w_{k1},\cdots,w_{kN}))$. By integrating the set of ODE in time from t to $t+T$ and by using the boundary condition $\boldsymbol{W}(t)=\boldsymbol{W}(t+T)$ the Floquet-exponents σ can be determined. The neutral surface $V_0(q,p,\omega)$ with respect to q and p provides the absolute threshold $V_c(\omega)$ and the critical wavevector (q_c, p_c). For a Hopf-bifurcation the critical frequency is defined by the Hopf frequency $\nu_c(\omega)=\mathrm{Im}\,[\sigma_{\max}(V_c(\omega), q_c, p_c)]$. The condition $\partial^2 V_0(\omega)/\partial p^2>0$ at $(q_c, p_c=0)$ is necessary for normal rolls $(q_c, p_c=0)$ to occur at threshold. Otherwise there exists a lower threshold at $p_c>0$ (oblique rolls). If there is continuous transition from normal to oblique rolls $p_c\to 0$ at threshold by changing the frequency the transition frequency $\omega\cdot\tau_0$ is then marked by $\partial^2 V_0(\omega)/\partial p^2=0$ at $(q_c, p_c=0)$ and we call this frequency the Lifshitz point.

For a vanishing flexoelectric effect and a driving voltage with the property $V(t+T/2)=-V(t)$, we now consider the symmetry behavior of the solutions of Eq. (2·1) in more detail. The symmetry of $\boldsymbol{u}'$ with respect to z is

$$(\Phi,\Theta,\Psi,v_x,v_y,v_z)(-z)=\pm(\Phi,\Theta,-\Psi,-v_x,-v_y,-v_z)(z) \tag{2·4}$$

(+sign="type I", −sign="type II") and the symmetry with respect to the translation $t\to t+T/2$ is

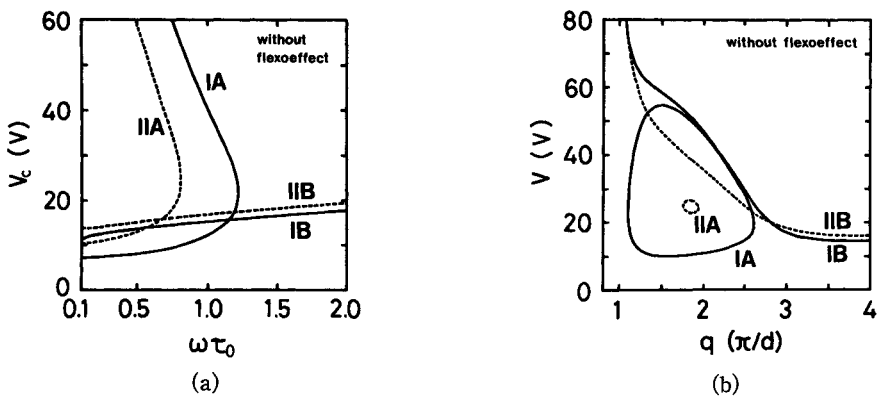

Fig. 2.1. Thresholds of four branches for solutions described in text; (a) minima of neutral curve as a function of frequency (b) neutral curves at frequency slightly below f_c.

Downloaded from https://academic.oup.com/ptps/article/doi/10.1143/PTPS.99.458/1882039 by guest on 21 August 2022

$$(\Phi, \Theta, \Psi, \boldsymbol{v})(t+T/2)=\pm(-\Phi, \Theta, \Psi, \boldsymbol{v})(t) \qquad (2\cdot5)$$

(+sign="type A", −sign="type B"). Type A is the well-known "conduction" mode and type B the "dielectric" mode. The symmetry (2·5) expresses also the fact that without the flexoelectric effect the polarity of the electric field E does not affect the director orientation $\boldsymbol{n}$ and the velocity $\boldsymbol{v}$. In each symmetry class one obtains a lowest threshold $V_c(\omega)$.

The thresholds $V_c(\omega)$ for these four solutions are shown in Fig. 2.1(a). They have been calculated for the material parameters of MBBA with $\sigma_\perp d^2=80\cdot10^{-8}\,\Omega^{-1}\,\mathrm{m}^{-1}(\mu\mathrm{m})^2$ and a harmonic driving voltage. Here $\sigma_\perp$ is the conductivity perpendicular to the director. The type IA solutions describe the lowest threshold in the low-frequency "conduction" regime whereas the type IB solutions provide the lowest threshold in the high-frequency "dielectric" regime. At these lowest thresholds one has always normal rolls ($p_c=0$). Type IIA and IIB solutions describe modes with higher thresholds. For the IA mode the threshold curve turns over to the upper restabilization branch at the so-called cutoff angular frequency ω_c. The IIA mode shows the analogous behavior. The two dielectric modes IB and IIB have different z-symmetry but the threshold-difference between both is relatively small, which is quite remarkable.

The threshold difference in-between the first two z-dependent modes (one symmetric and another anti-symmetric with respect to the thickness d of a layer) in conventional R-B convection in simple fluids and also the threshold-difference between the modes IA and IIA is of the order of the first threshold value. Therefore an interaction of these two simple modes could only be expected far away from the threshold but then already also higher harmonics in the z-direction are excited and the nonlinear solution becomes complicated. However the small difference in the threshold between the IB and IIB modes can be considered as an unfolding of a codimension-two (CDT)-bifurcation where a simple interaction of both modes is possible. The behavior is perhaps reasonable for the occurrence of the chevron structure discussed in § 5. The associated critical wavenumbers for the IB and IIB modes are also similar and are both nearly proportional to $\sigma_\perp$ at a fixed frequency $\omega\tau_0$. The critical wavenumbers of the conduction modes are nearly insensitive to the change of $\sigma_\perp\cdot d$. The detailed behavior of the neutral curves is discussed elsewhere.[35]

In order to look in a different prospect on the four modes we have plotted the neutral curves for the frequency $\omega\cdot\tau_0=0.8$ ($\tau_0=\varepsilon_0\varepsilon_\perp/\sigma_\perp$ is the charge relaxation time where ε_0 is the dielectric constant of the vacuum)[20)~22)] in Fig. 2.1(b). The neutral curves of the branches IA and IIA are closed loops in the frequency range with restabilization. The growth rates are positive inside the loops. The neutral curves for the branches IA and IB and also IIA and IIB respectively are in general not allowed to intersect each other. This explains the deformation of the neutral curve in IB. By intersecting $\sigma_\perp d$ the threshold of the dielectric mode increases strongly and then this deformation can be removed.

The intersection point of the lowest threshold curves $V_c(\omega)$ in Fig. 2.1(a) corresponds to the situation where in Fig. 2.1(b) the minima of two lowest curves (IA and IB) lie at the same voltage. This is the situation of a CDT-bifurcation of two

Downloaded from https://academic.oup.com/ptps/article/doi/10.1143/PTPS.99.458/1882039 by guest on 21 August 2022

bifurcations with different wavenumbers. At this CDT-point the wavenumber ratio q_c^d/q_c^c of the dielectric and the conduction mode can vary over a large range ($\sim$1-20) depending on the parameters, especially the dielectric anisotropy, the conductivity and thickness and the externally changeable magnetic field. By an appropriate choice of $\sigma_\perp d$ and an additional easily-adjustable-stabilizing-magnetic-field in the x-direction the ratio q_c^d/q_c^c can be also brought to the resonance value 2 to 3. Near such a CDT-point various interesting secondary bifurcations are expected.[37] The detailed character of the CDT-point, however, also depends on whether the threshold $V_c(\omega)$ of the dielectric mode intersects the conduction threshold at the lowest branch or at the restabilization branch or at the turn-over point (see Figs. 2.1 and 5.4 on typical threshold as a function of ω). The differences between these last three possibilities become stronger for a nematic material with large negative dielectric anisotropy $\varepsilon_a=\varepsilon_{/\!/}-\varepsilon_\perp$.[38]

Taking the flexoelectric effect into account the separate symmetries (2·4) and (2·5) are destroyed, but the combined symmetries $z\to -z$ and $V\to -V$ remain. That means for driving voltages with the symmetry $V(t+T/2)=-V(t)$ one still has two separate modes: The superposition of type IA and IIB solutions provides the threshold for the conduction regime and the superposition of the type IB and IIA solutions gives the threshold for the dielectric regime. Using a driving voltage without the above symmetry a superposition of all four types is necessary to solve the linear problem and therefore no further a priori distinction between the conduction and the dielectric mode is possible.

The calculations of the threshold behavior obtained from the full set of hydrodynamic equations can be also extended to stochastic excitations. Due to the stochastic excitations the described independent linear threshold modes are coupled. It is an open question whether this leads for example to a Hopf bifurcation or to a multiple bifurcation point, where the real parts of several eigenvalues pass simultaneously through zero. In an experiment it has been found that by a stochastic excitation it is possible to induce a direct transitions from nonconvective to turbulence.[39),57]

§ 3. Defect turbulence (fluctuating Williams domain)

At a first instability point V_c, WD appears which shows stationary stripe patterns.[15),16] For slightly larger voltage-step than V_c from $V=0$, typically $\varepsilon\sim 0.2$, a defect can be observed. Here ε is the normalized deviation from V_c, i.e., $\varepsilon=(V^2-V_c^2)/V_c^2$. It is very important to investigate a single defect motion for construction of model equations in amplitude and phase as described previously.[19] In this section we will discuss on this state called FWD. Figure 3.1 shows a series of its spatial power spectra in the x-direction parallel to the original director orientation (rubbing direction). These are plotted after averaged over 400 spectra taken along the y-direction. Two sharp peaks (one is harmonics of another) is due to unequal brightness of roll convections for up- and down-flows. (This could be adjustable experimentally.) The structure change in the spectra is clearly observed here. There is hysteresis at the transition from WD to FWD in small aspect ratio (Γ) systems.[19] To quantize the hysteresis, the similarity intensity factor (SI) is calculated with the relation,

Downloaded from https://academic.oup.com/ptps/article/doi/10.1143/PTPS.99.458/1882039 by guest on 21 August 2022

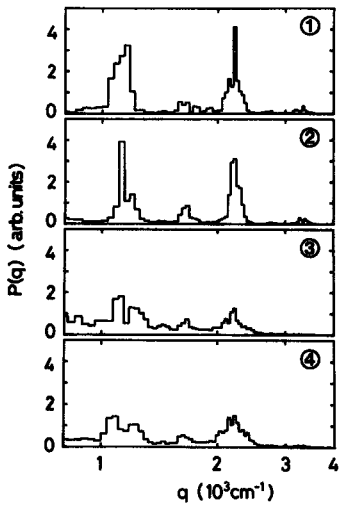

Fig. 3.1. A series of power spectra in WD to FWD increasing (1, 2) and decreasing (3, 4) in voltage. 1 and 4 are the same value of V (see Fig. 3.2(b): the location is marked). The power spectra for 2 and 4 show a clear hysteresis in their structures.

$$\mathrm{SI}=1/((1/N)\sum_{i}^{N}(P_u(q_i)-P_d(q_i))^2) \tag{3·1}$$

for both ways of increase (P_u) and decrease (P_d) of the electric voltage, which is originally used in order to characterize turbulence by difference between power spectra for two different directions, along x and y.[40),41)] Here N is the summation number of wavenumber q_i. The integral intensity $\Sigma P(q_i)$ over twenty wavenumbers around a maximum peak-wavenumber with the resolution 36.4 cm^{-1} is also calculated. This value therefore means the broadness of the spectrum peak. These are shown in Fig. 3.2(a) for SI and Fig. 3.2(b) for the integral intensity. The larger the SI, the more similar the power spectrum. Namely it suggests no hysteresis when SI is always very large. The result clearly shows the hysteresis of which width in this sample was about 1V ($\Delta\varepsilon\sim0.2$). To determine the width, a slow enough ramp rate is needed since it depends on a ramp rate effectively and also on Γ. In FWD regime, spatio-temporally complicated defect motions can be observed. Such spatio-temporal motions are shown in Fig. 3.3 for large Γ and for different ε. Here gray level of a video image is plotted taking one scanning line perpendicular to the original roll axis against time. For small ε, still periodic structures can be recognized. As increasing ε, however, the spatio-temporal pattern of defect motions becomes complicated and no periodic pattern can be observed for $\varepsilon=1.23$.[19)]

Figure 3.4 shows the temporal variation of the number of defects in FWD. It

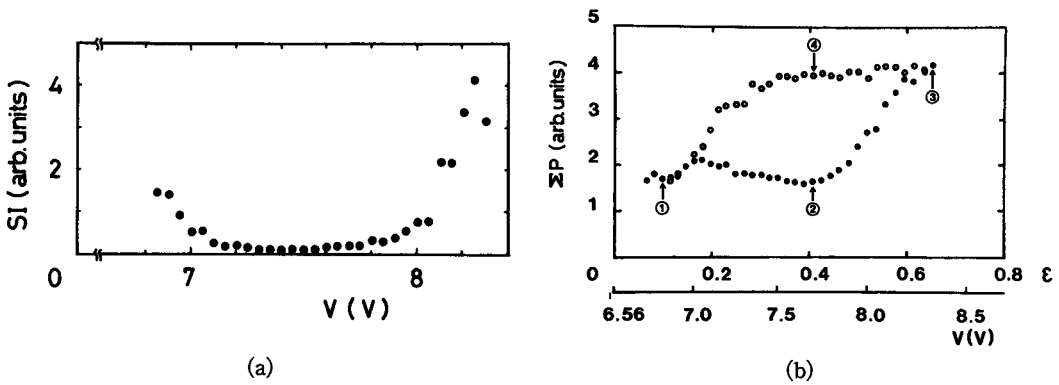

(a) (b)

Fig. 3.2. Quantitative estimation for hysteresis in FWD by SI (a) and by the integrated power spectrum (b). The ramprate is 5 mV/s and all image are recorded onto a magnetic disk and a tape simultaneously.

Downloaded from https://academic.oup.com/ptps/article/doi/10.1143/PTPS.99.458/1882039 by guest on 21 August 2022

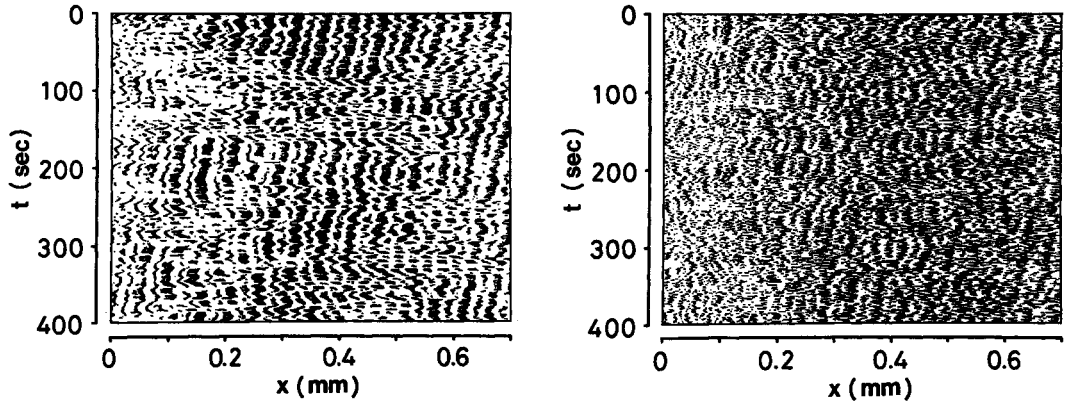

Fig. 3.3. Spatio-temporal map in FWD (d=50 μm and Γ=120×120). (a) ε=0.36, (b) ε=1.23.

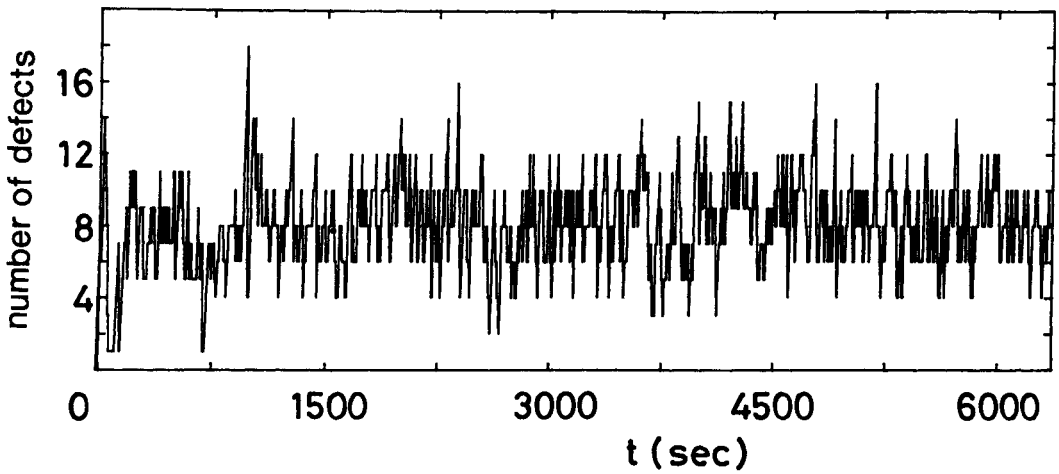

Fig. 3.4. Nonperiodic change in time for the number of defects (ε=0.60, f=10 Hz, f_c=61 Hz, Γ=10 ×15, d=100 μm).

changes nonperiodically and shows the $1/f$-type spectrum, which has been already discussed in detail.[19] In small Γ samples, $1/f$-type spectrum is always observed whereas in large Γ ones it is often white except at very small ε (where it is $1/f$-type). This suggests that $1/f$-spectrum may originate from boundary effects. A sequence of such nonperiodic signals always changes when several runs are done by repeating an application of a constant voltage $V > V_c$ in a step-like fashion from a non-convective state (Fig. 3.5). In Fig. 3.5 four different runs are displayed, where the initial numbers of defects are, for example, N_0=6, 4, 1 and 5 for (a), (b), (c) and (d) for ε=0.50 (left figure) respectively. Two cases were odd numbers of N_0, but odd number is not stable and the even number state is preferred. In order to obtain a dimensionality of nonlinear behavior, the correlation integral $C(r_x)$ is calculated by use of the relation,

Downloaded from https://academic.oup.com/ptps/article/doi/10.1143/PTPS.99.458/1882039 by guest on 21 August 2022

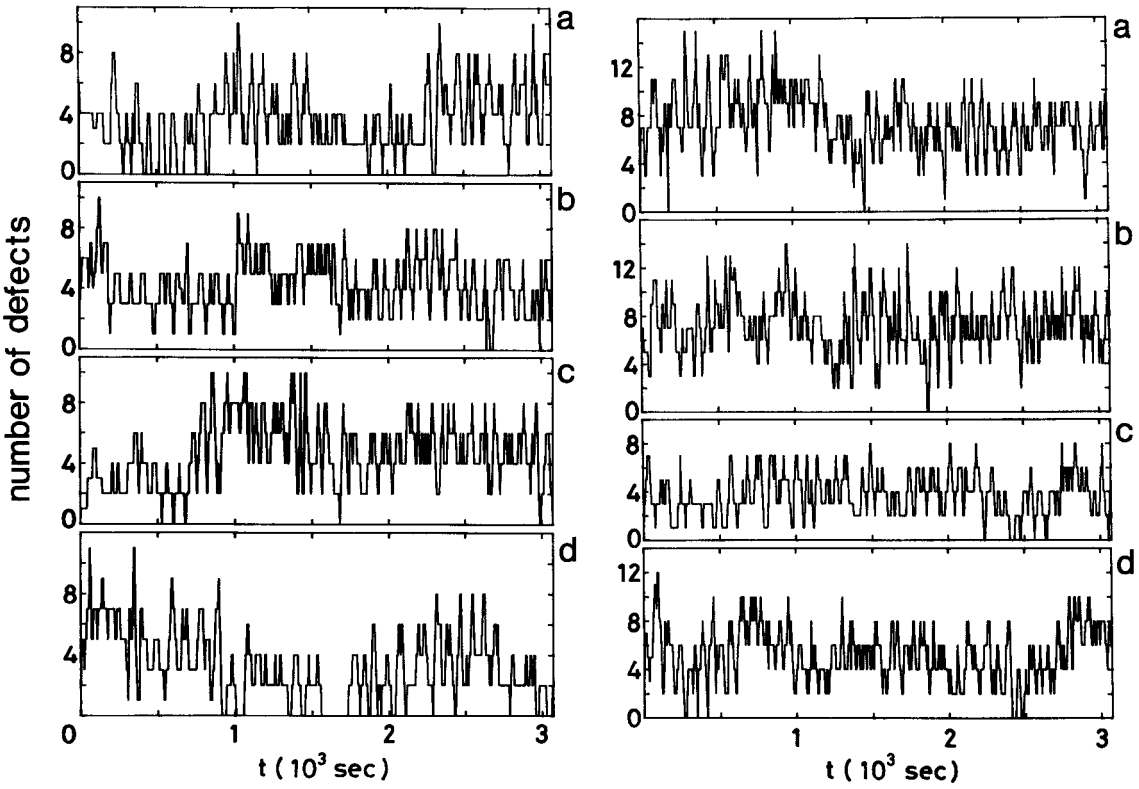

Fig. 3.5. Temporal changes of defect number for different runs. The same sample as in Fig. 3.4. (ε=0.50 (left) and 0.55 (right))

$$C(r_x)=(1/N)^2\sum_{i,j}^{N}H_V(r_x-(x_i-x_j))\sim r_x^{\nu}\,, \tag{3·2}$$

where N is the total number of vector x_i which is the n-component-vector with an embedding dimension n created by the embedding procedure,[42] $H_V(\xi)$ the Heviside function, r_x the distance between the corresponding vectors and ν the correlation dimension of nonlinear dynamical systems considered here. The elements of the vector x_i consist of a set of defect numbers obtained from repetition of time shifts with a constant time-delay in the nonperiodic change of the defect number.[42]

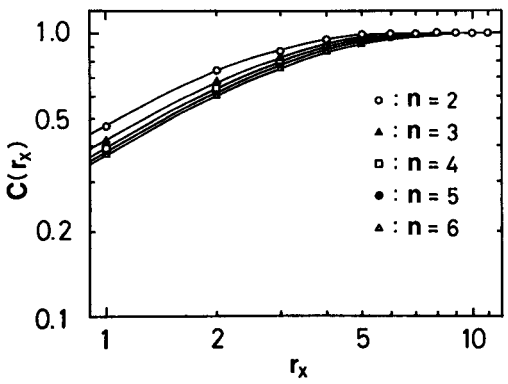

Fig. 3.6. Correlation integral $C(r_x)$ calculated for the data at ε=0.55 in Fig. 3.5.

The calculated result is shown in Fig. 3.6. Unfortunately, no determination of dimensionality was possible from this result because of the low resolution, but probably it is expected to be around 4 to 6 from it. Thus the defect chaos (FWD) may have a relatively low dimen-

Downloaded from https://academic.oup.com/ptps/article/doi/10.1143/PTPS.99.458/1882039 by guest on 21 August 2022

Table I. Mean interval of event for change in defect numbers (measured for entire area of samples).

	total time of observation	number of event	mean interval of event	mean number of defects
ε	T_t(sec)	N_{ev}	T_m(sec)	N_d
0.45	3066	189	16.2	3.14
0.50	22710	1447	15.7	4.07
0.55	15330	1480	10.4	6.33
0.60	6294	651	9.7	7.80

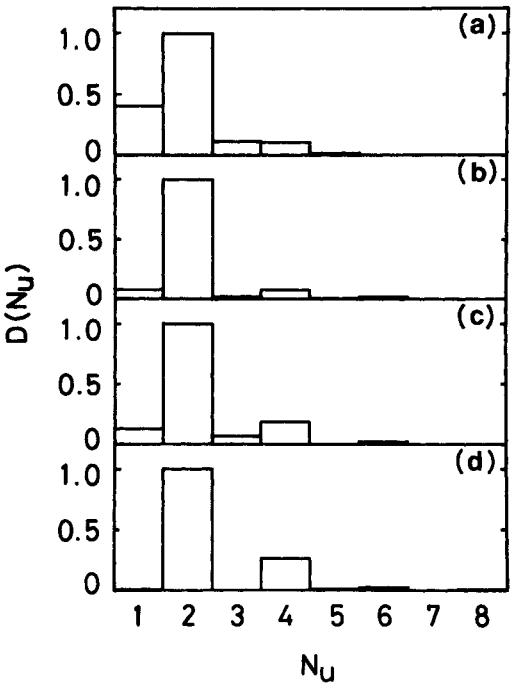

Fig. 3.7. Histogram of defect number changing in one event. The distributions are normalized by the maximum number N_{max}. ε=0.45 (N_{max} =116), 0.50 (N_{max}=1213), 0.55 (N_{max}=1050) and 0.6 (N_{max}=505) from the above. The each time gap of events in the measurements was 6 s.

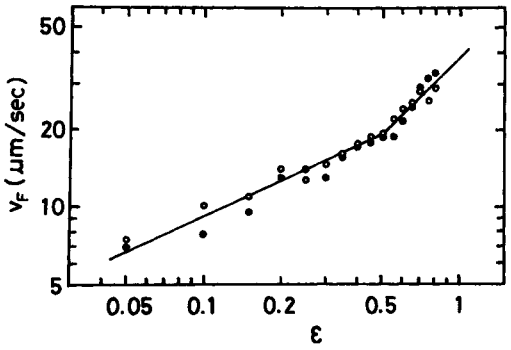

Fig. 3.8. Front propagation velocity v_F in WD and FWD as a function of ε (d=100 μm, Γ=14×9). The slope changes from 0.5 to 1 at ε~0.5 where FWD is observed in the steady state.

sional attractor for small Γ.[12] The better resolution and the larger number of defects can be obtained for the larger Γ. However the dimension of attractor in that case would be different from that for small Γ.

In order to understand defect chaos more detailedly, a statistical analysis for defect numbers has been done. The total number N_{ev} of events of defect change and distribution of the number of changing defects at each event are evaluated. The mean interval T_m ($=T_t/N_{ev}$) for the events changing a defect number is shown in Table I, where T_t is a total observation time. Obviously, T_m decreases with increase of ε, that means the event of defect-number-change happens more frequently for larger ε. The more detailed content of the events is shown in Fig. 3.7 as a frequency

Downloaded from https://academic.oup.com/ptps/article/doi/10.1143/PTPS.99.458/1882039 by guest on 21 August 2022

distribution of the defect number which changes simultaneously at each one event. As seen from this, increasing ε the number of pairs for nucleation and annihilation happening at the same time increases. The distribution for nucleation shows similar profile with one for annihilation. Annihilation and nucleation tend to happen with pairs whose number increases with ε (see Fig. 3.7).

The velocity v_F of front propagation of roll convections in FWD ($\varepsilon > 0.5$) has ε-dependence like $v_F \sim \varepsilon$ different from that ($v_F \sim \varepsilon^{0.5}$) in WD region (Fig. 3.8). This suggests that the amplitude equations in FWD must have different forms from those in WD. Similar behavior was observed in growth time and other dynamical factors.[23),43)]

§ 4. Local transition between turbulent states DSM1 and DSM2

If the voltage is increased further, after a sequence of transitions, the turbulence, the dynamic scattering mode (DSM), appears.[6),15),43)] Visual observations have already shown in early time that there are two different kinds of DSM in planar orientation as well as homeotropic NLC, the DSM1 and the DSM2 states. DSM2 occurs at the higher voltage (above the threshold voltage V_2). Both states have been characterized in planar orientation more quantitatively by measuring the spatial power spectra of the transmitted light through a sample parallel ($P_{/\!/}$) and perpendicular ($P_\perp$) to the original undistorted-director orientation. $P_{/\!/}$ and $P_\perp$ have different structures in the DSM1 state and become similar in the DSM2 state. Therefore we used the notion, anisotropic (DSM1) and isotropic turbulence (DSM2).[41)] According to the early studies achieved by us[24),43)] and others,[44)~47)] a large jump in the light transmittance (LT) at V_2 has been called traditionally the DSM1-DSM2 transition. Such large changes in LT can be observed only at two different voltages, V_c and V_2.

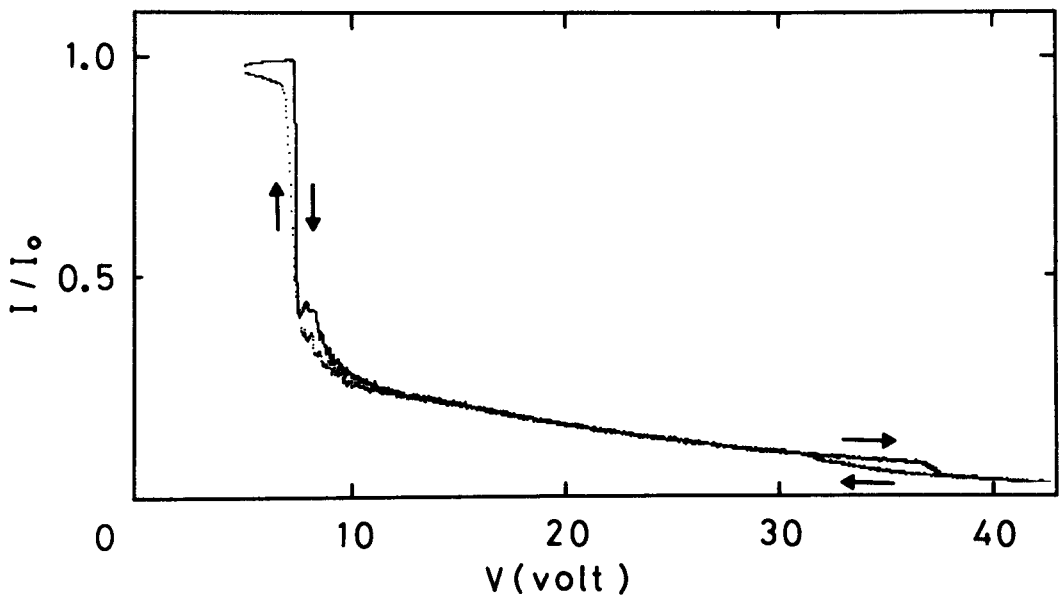

Fig. 4.1. Light transmittance LT($=I/I_0$) through sample for increasing and decreasing applied voltage with the ramp-rate $r=0.025$ V/s. I_0 is the light intensity in the absence of convection.

Downloaded from https://academic.oup.com/ptps/article/doi/10.1143/PTPS.99.458/1882039 by guest on 21 August 2022

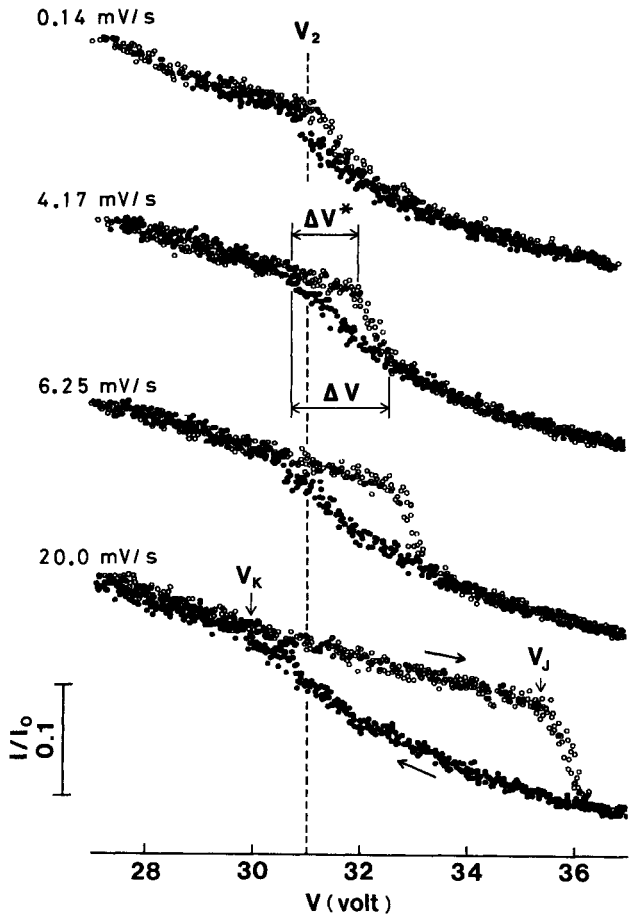

Fig. 4.2. Hysteresis in I/I_0 near the DSM1-DSM2 transition for various ramp rates r (mV/sec). We choose two different hysteresis gaps ΔV and $\Delta V^*(=V_J-V_K)$.

In some our previous publications,[14),17),40),41)] we called the latter point the DSM like-DSM1 transition. As this makes large confusing, we obey the conventional naming, the DSM1-DSM2 transition, hereafter.[48)]

Figure 4.1 shows the light transmittance LT $(=I/I_0)$ through the sample as a function of an increasing and decreasing applied voltage, where the ramp rate $r=0.025$ V/s has been used. I_0 is the light intensity passing through the sample in the absence of the convection. There are two clear jumps (accompanied by hysteresis) in LT, as already shown in early studies.[41),43)] The hysteresis which depends on r is shown for the latter transition enlarged in Fig. 4.2 for different r. It can be uniquely recognized that the hysteresis gap ΔV shrinks with decreasing r and shows a square root dependence on r (see Fig. 4.3),[48)]

$$\Delta V=(C_h r)^{1/2}. \tag{4·1}$$

The solid line in Fig. 4.3 is calculated from Eq. (4·1) with the constant $C_h=1.780\times10^3$

Downloaded from https://academic.oup.com/ptps/article/doi/10.1143/PTPS.99.458/1882039 by guest on 21 August 2022

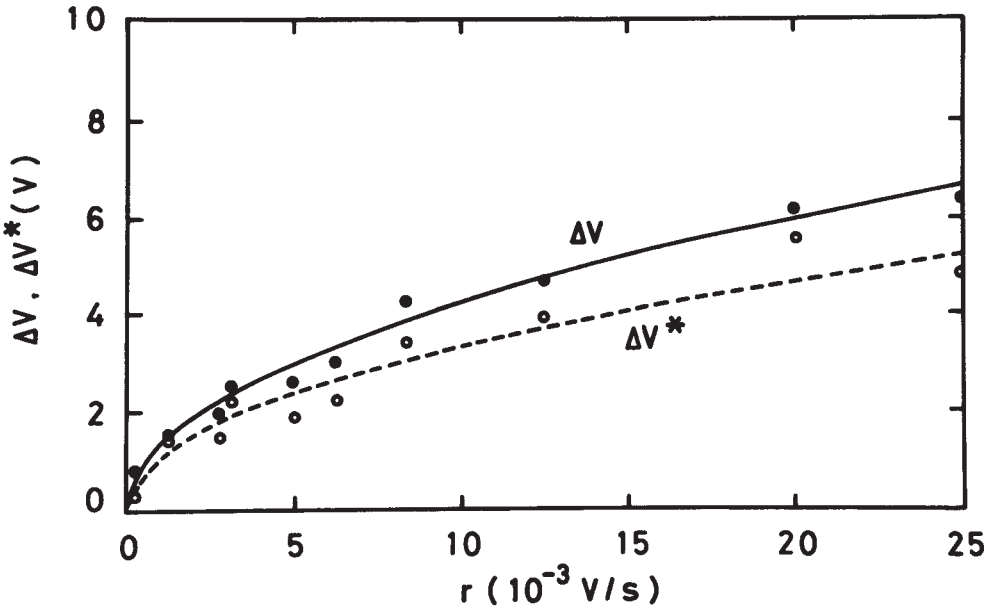

Fig. 4.3. Dependence of hysteresis-gaps ΔV and ΔV^* in LT (as defined in Fig. 4.2) on ramp-rate r (mV/s). The solid curve shows Eq. (4·1) for ΔV with $C_h=1.78\times10^3$ and the dotted curve for ΔV^* with $C_h=1.09\times10^3$ Vs.

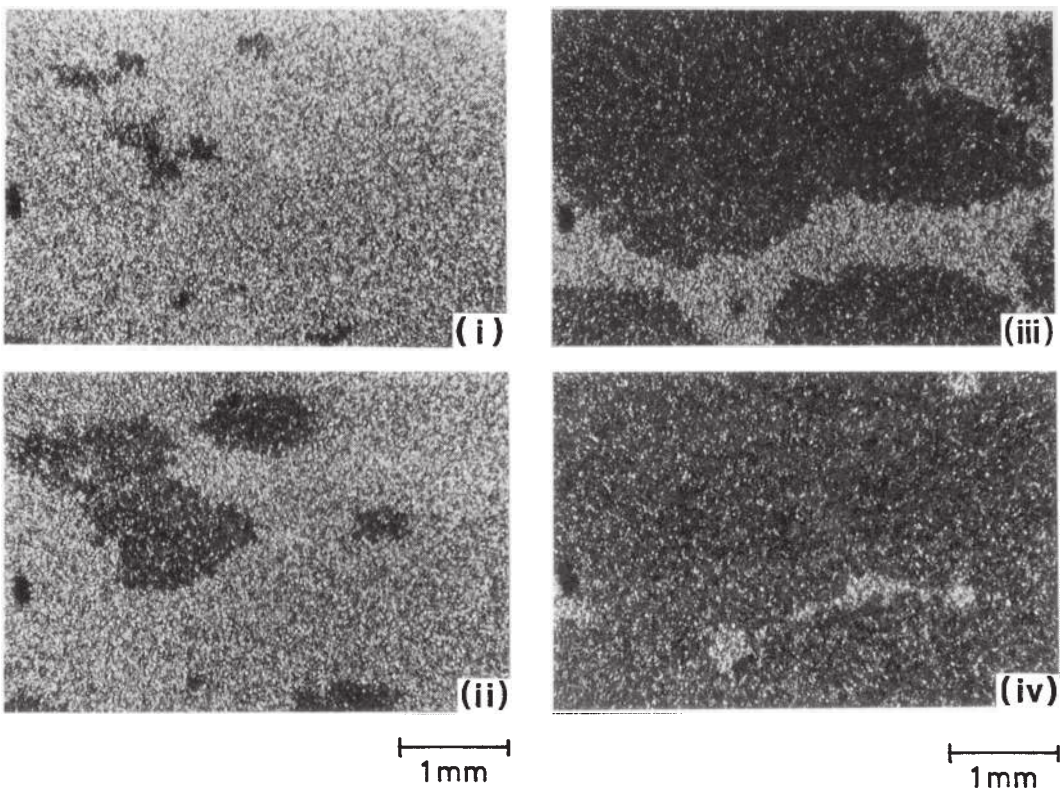

Fig. 4.4. (continued) (a) $\varepsilon_2=1.04$

Downloaded from https://academic.oup.com/ptps/article/doi/10.1143/PTPS.99.458/1882039 by guest on 21 August 2022

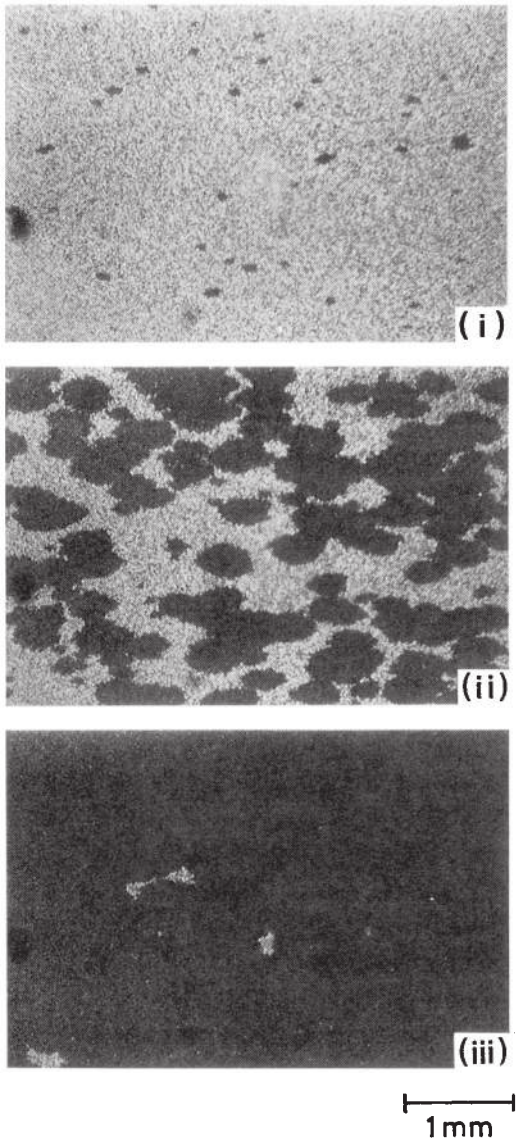

(b) $\varepsilon_2=8.0$

Fig. 4.4. A set of photographs for growth process of DSM2-nuclei at different times after applying a voltage larger than DSM2 threshold voltage V_2. In (a) $\varepsilon_2=1.04$, (i) $t=15$s, (ii) 35s, (iii) 65s, (iv) 100s and in (b) $\varepsilon_2=8.0$, (i) $t=1$s, (ii) 3s, (iii) 6s.

in units of volt-second. Figures 4.2 and 4.3 indicate that the DSM1-DSM2 transition is of second order (forward bifurcation) unlike our conclusion in a previous publication where we used only one finite ramp rate.[41] The threshold voltage V_2 for the DSM1-DSM2 transition is determined by crossing of LT curves in Fig. 4.2 at the lower voltage (see Fig. 4.2), which is nearly independent of r and we find $V_2=31$V ($V_2/V_c\sim4.6$).

A set of photographs for the growing nuclei is shown in Fig. 4.4 in two typical cases for $\varepsilon_2=1.04$ and for 8.0, where $\varepsilon_2=(V^2-V_2^2)/V_2^2$ measuring the distance from the threshold V_2 for the DSM2 state. For the value 8.0 a large number of nuclei can be seen in contrast to the case for 1.04. A very similar type of growth processes has been already reported in polarization reversal domains of ferroelectric LCs,[49] which is a non-convective system (there is no contradiction between no hysteresis (supercritical bifurcation) and occurrence of nucleation because nucleation always happens at deep quench in any case).

According to the fact that our transition is local, we look in more detail on the similarities with common nucleation phenomena. In Fig. 4.5 we show the nucleation rate J of the DSM2 turbulent nuclei, which we obtain by counting these spontaneous nuclei at a few seconds after jumping from $V=0$ to voltages above V_2. The solid line is obtained from a common expression,[48),50]

$$J=J_\infty\exp(-A/(1+\varepsilon_2))+B\,, \quad (4\cdot2)$$

where the values of $J_\infty=920\ \mathrm{mm}^{-2}$, $A=50$ and $B=1.4\mathrm{mm}^{-2}$ for 27 °C and 800, 25 and 0.9 for 32 °C respectively, have been obtained for the best fit of Eq. (4·2) to the data in Fig. 4.5. Here A corresponds to the potential difference between DSM1 and DSM2 states. B is probably related to the contribution from a heterogeneous nucleation, induced,

Downloaded from https://academic.oup.com/ptps/article/doi/10.1143/PTPS.99.458/1882039 by guest on 21 August 2022

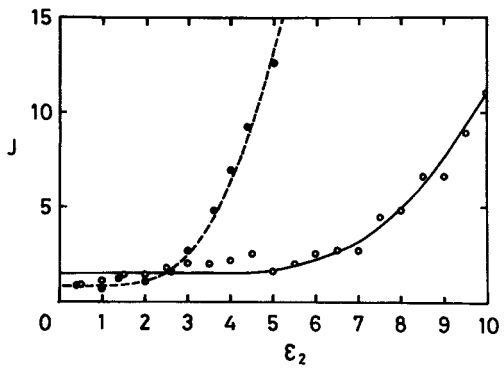

Fig. 4.5. Nucleation rate J for DSM2-turbulent nuclei as a function of ε_2 at two different temperatures. ○: 27 °C, ●: 32 °C. The solid and the dotted curves are due to Eq. (4·2).

e.g., by big nucleation sites on the surface electrodes. $J_\infty = 920\ \mathrm{mm}^{-2}$ gives a corresponding value $33 \times 33\ \mu\mathrm{m}^2$ to the minimum area for one nucleation phenomenon. This size $33\ \mu$m coincides with the value $d/\sqrt{2}$, which probably suggests the absolutely minimum size for a critical nucleus of disclination domain. This will be restricted by the elastic deformation energy in director field. The homogeneous nucleation occurs rather stochastically when the experiments are repeated after long enough relaxation time. Figure 4.6 shows the scaling property of DSM2 area summed over all nuclei by use of the Kolmogorov-Avrami equation.[49] There is clear scaling of growth kinetics of nuclei. The index 2.5 in t means that the nucleation rate is not constant in time and gradually decreases because the growth velocity is experimentally constant in time. In the present transition phenomenon, a statistical theory for crystal growth can be suitably used.

The main difference between the DSM1 and the DSM2 states is the density of disclinations in the director field, which is much higher in the DSM2.[48] To visualize this, we use the fact that both relaxations of the velocity field and the simple director distortions are much faster than the relaxation of disclinations.[24] Switching off the applied voltage $V > V_2$ at a time when the DSM2 state has already filled considerable space (Fig. 4.7(a)), then the disclinations can be clearly observed in the area of the DSM2 before, as shown in Fig. 4.7(b) and enlarged in Fig. 4.7(d). Switching on again the voltage to above V_2, before the disclinations have been vanished, then the disclinations serve as nucleation centers for the DSM2 state (Fig. 4.7(c)). The disclination density itself increases with ε_2.

The DSM2-nuclei grow self-similarly until fusion with other nuclei. During the growth of the DSM2 nuclei continuously new disclinations are created. The disclina-

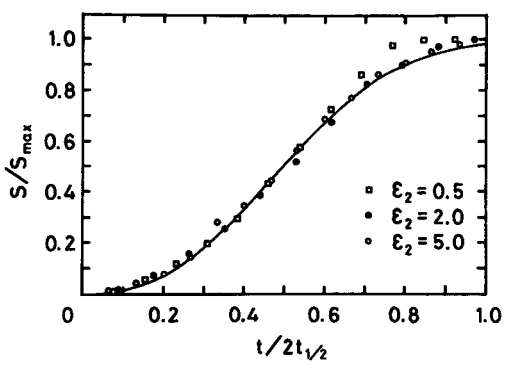

Fig. 4.6. Scaled temporal evolution of total area of DSM2. $t_{1/2}$ is the time at which half the area is covered by DSM2 state. Here S and S_{max} show total area of DSM2 and total observed area, respectively. The solid line shows the equation,

$$S/S_{max} = 1 - \exp[-Kt_N^{2.5}],$$

assuming constant nucleation rate, constant growth velocity and a two dimensional growth in Kolmogorov-Avrami theory.[49] Here the index 2.5 of t_N means that nucleation rate should not be constant and decreases with time. K is constant due to constant growth velocity and nucleation rate, and $t_N = t/t_{1/2}$.

Downloaded from https://academic.oup.com/ptps/article/doi/10.1143/PTPS.99.458/1882039 by guest on 21 August 2022

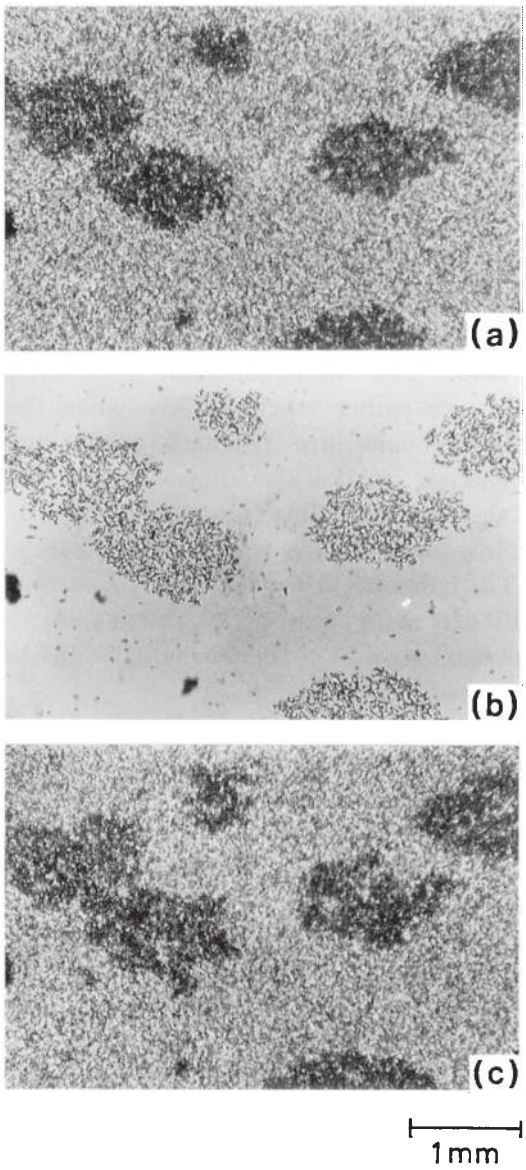

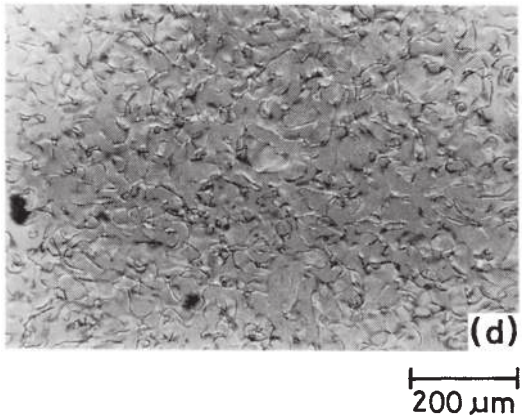

Fig. 4.7. Retriggering process of the DSM2 state by disclinations. Photographs (a), (b) and (c) are taken times after jumping with the applied voltage above the DSM2 threshold V_2; $\varepsilon_2=1.04$. (a): $t=24$s after application of the voltage. (b): $t=26$s immediately after the field is switched off. (c): $t=28$s immediately after the field is applied again. (d) is an enlargement of a disclination domain. In photograph (b), a large number of disclinations can be seen in the domain where the DSM2 flow existed before. It can be recognized from (c) that disclinations serve as nucleation centers for the DSM2 domains.

tion density inside the nuclei keeps roughly constant. By measuring the diameters in both main directions of the elliptical nuclei as a function of time, we always determined the growth velocity in a range where it was rather independent of the diameter. The ε_2-dependence of the velocity parallel ($v_{/\!/}$: open circles) and perpendicular ($v_\perp$: solid circles) to the original director-orientation is shown in Fig. 4.8 for the temperatures 27 °C and 32 °C. The solid lines show the expression $v=\gamma\cdot\varepsilon_2^{0.7}$, whereas γ has been chosen for the best fit with the values: $\gamma=54$ μm/s ($v_{/\!/}$ at 27 °C), 29 μm/s ($v_\perp$ at 27 °C), 65 μm/s ($v_{/\!/}$ at 32 °C), 35 μm/s ($v_\perp$ at 32 °C). The velocity ratio $v_{/\!/}/v_\perp=1.85$ is rather independent of ε_2 and is equal to the ratio of the diameters along the long and the short axes of the elliptical nuclei. The growth velocity becomes slow as decreasing ε_2 and tends to zero as ε_2 goes to zero. This tendency well agrees with that of the

Downloaded from https://academic.oup.com/ptps/article/doi/10.1143/PTPS.99.458/1882039 by guest on 21 August 2022

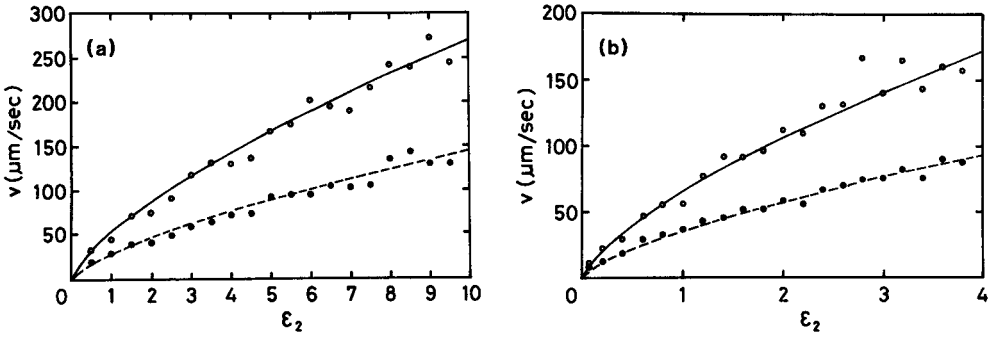

Fig. 4.8. Growth velocity of DSM2 nuclei parallel $v_{/\!/}$ (solid lines) and perpendicular $v_{\perp}$ (dots) to the original orientation of director as a function of ε_2 for 27 °C (a) and 32 °C (b). The given curves are due to $\gamma\varepsilon_2^{0.7}$, with γ=54 μm/s ($v_{/\!/}$, 27 °C), 29 μm/s ($v_{\perp}$, 27 °C), 65 μm/s ($v_{/\!/}$, 32 °C) and 35 μm/s ($v_{\perp}$, 32 °C).

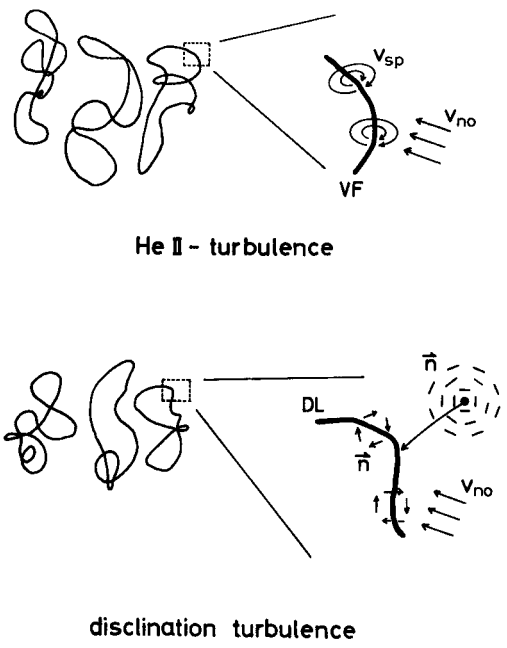

Fig. 4.9. Schematic drawing of analogy between disclination in EHD and vortex filament in HeII turbulence. It can be said that the director deformation field around DL in EHD corresponds to the vortex field of superfluid around VF in the present analogy.
DL: disclination line, $\boldsymbol{n}$: director field, $\boldsymbol{v}_{n0}$: velocity field of normal fluid, $\boldsymbol{v}_{sp}$: velocity field of superfluid, VF: vortex filament.

growth and the relaxation times of DSM 2 as has been already reported in Ref. 14) where both times have divergent tendency in proportion to $\varepsilon_2^{-0.68\pm0.1}$.

It is not possible to reverse the growth velocity of the nuclei by decreasing ε_2 below zero, instead the DSM2 state disperses globally away. In that respect the motion of the DSM1-DSM2 interface of the nuclei resembles propagating fronts in other systems above a supercritical bifurcation,[51] which would be in agreement with our LT measurements. The front velocity at a supercritical bifurcation $v_s=\tau\varepsilon_2^{0.5}/\xi_c$ (where τ is a characteristic time and ξ_c is the coherence length) however, does not fit our experimental data although many tries have been done. This is also the case for the front velocities from other deterministic equations related to the subcritical or transcritical bifurcations (as discussed in Ref. 51)) and simple extensions of those. At the DSM1-DSM2 bifurcation, mainly the disclination density is changed, indicating that it is the relevant order-parameter. The flow field in both DSM regions is turbulent and due to our observations the disclinations are presumably by strong short range fluctuations through viscous coupling between the director and the flow field. The relevant control parameter in this picture would be the flow field,

Downloaded from https://academic.oup.com/ptps/article/doi/10.1143/PTPS.99.458/1882039 by guest on 21 August 2022

which works rather stochastically for the disclinations. Therefore a realistic model for the DSM1-DSM2 interface motion must at least include a stochastic part in the control parameter or some additive noise components,[52] in contrast to the available deterministic models, if not an *ab initio* approach, starting from the basic equations of EHD will be necessary.[21]

The reported local transition (nucleation type) between the two turbulent states DSM1 and DSM2 is rather uncommon for convective systems.[53),54] In the early stage of the bifurcation there is surprising similarity to other well-known nucleation processes in nonconvective systems, whereas, besides the mentioned difference, the late stage of the growing nuclei is more comparable with propagating fronts in other nonequilibrium systems. The main feature due to the DSM1-DSM2 transition is the change of the disclination-density in the director field. This property, addition to the previously reported facts; the divergence in the relaxation time[14] and the drastic increase in the fluctuation amplitude[55] at the DSM1-DSM2 bifurcation point, is quite similar to the properties of the TI-TII transition in superfluid HeII, where the vortex filament density is changed due to the bifurcation.[25] In this respect, the disclination density in EHD will correspond to the density of quantized vortex filaments in HeII turbulence (see Fig. 4.9), that is the field for superfluid is replaced by the director field. The vortex of superfluid and the vortex-filament in HeII correspond to the rotation of director and the disclination line in EHD respectively. We can call therefore DSM2 the disclination turbulence. We hope that the presented transition stimulates further investigations, which can be complementary as well as extending to the studies of superfluid turbulence in HeII. Especially the influence of multiplicative noise of the transition seems promising,[56),57] because it can be applied also in our system in a well-controlled manner.[57]

§ 5. Chevron pattern: Periodic defect orientation in the dielectiric regime

The main difference between the dielectric regime and the conduction regime in EHD convection is that the director and the velocity field should be roughly stationary in the conduction regime (low frequency), besides some modulation, and oscillatory with the external frequency in the dielectric regime. The opposite should be the case for the charge density.[31),32),58] Often in the dielectric regime at threshold one observes a short-wavelength stripe pattern which aligns normal to the undistorted director orientation.[6] The oscillatory behavior of the director in this pattern has been shown by observing the temporal behavior of the transmitted light signal as described in Ref. 58). Above the primary instability a secondary transition to a herringbone structure, the so-called chevrons, occurs. The transition behavior from the stripe to the chevron pattern will be considered in the following.

The pictures of Fig. 5.1 give an example how the pattern changes to chevrons.[19] Immediately above threshold the periodic pattern looks as shown in Fig. 5.1(a). Experimentally it was observed that the convection accompanying this periodic structure takes place in a skin layer.[17),28] The bifurcation from the unstructured state is supercritical and also the bifurcation to the chevrons. Just above threshold one observes very narrow WD and a finite defect density with similar behavior as

Downloaded from https://academic.oup.com/ptps/article/doi/10.1143/PTPS.99.458/1882039 by guest on 21 August 2022

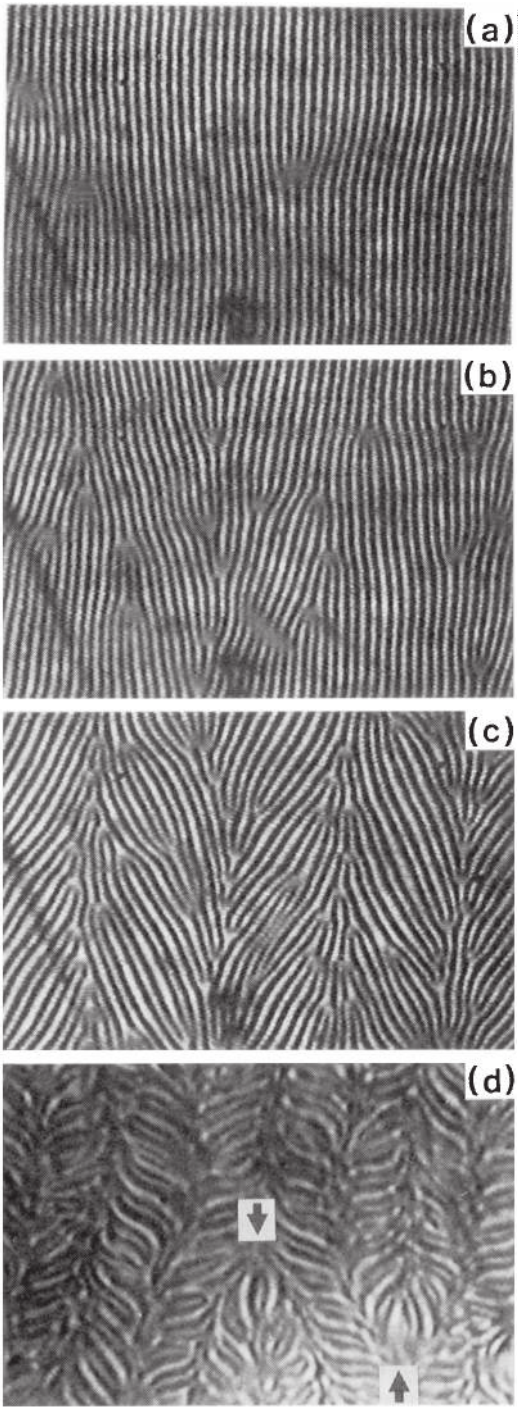

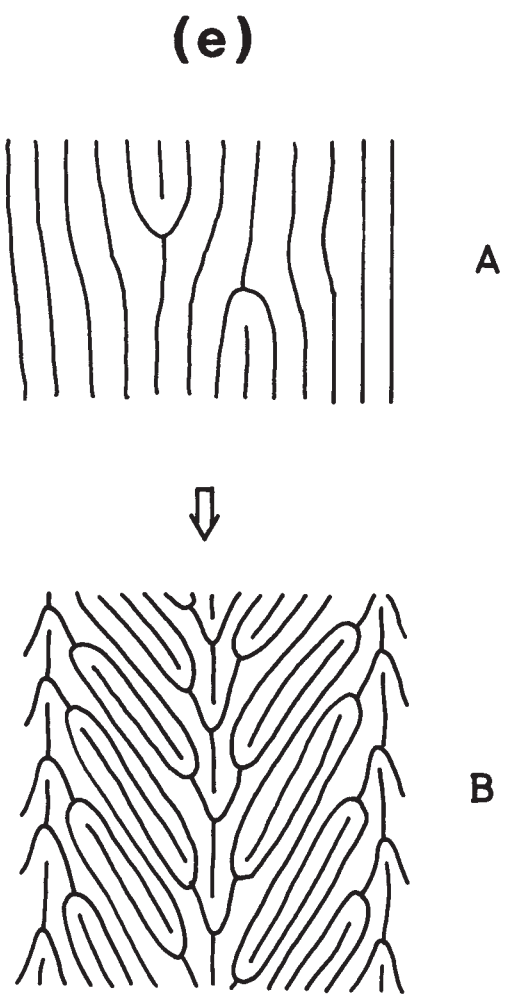

Fig. 5.1. Formation process of the chevron pattern. Applied voltage of $f > f_c$ is increased from (a) to (d). (e): schematic drawing of defect orientation for (c). The arrows in (d) indicate the macroscopic defects in new scale. A: defects in for example FWD. B: chevron structure (periodic-defect orientation).

described above for FWD. Here defects glide very fast and over a wide range (Fig. 5.1(a)). This density is changing in time and one observes always a dynamic behavior of the defects. By increasing the applied voltage in a steady manner beyond the threshold, the total defect number increases and the defect-density becomes locally

Downloaded from https://academic.oup.com/ptps/article/doi/10.1143/PTPS.99.458/1882039 by guest on 21 August 2022

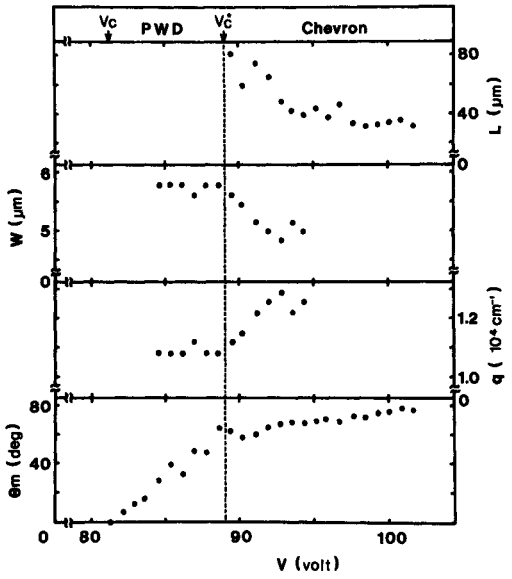

(a)

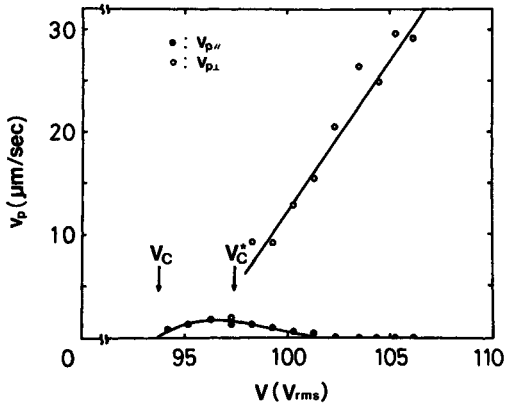

(b)

Fig. 5.2. Wavelengths w of rolls, L of periodic defect line, and maximum inclination angle θ_m (a), and propagating velocities of PWD and chevron (b) as a function of applied voltage. (c) definition of w, L, θ_m and v_p. $v_{p//}$ and $v_{p\perp}$ are the velocities parallel and perpendicular to the original director orientation. In (b) the frequency of an applied voltage is different from in (a).

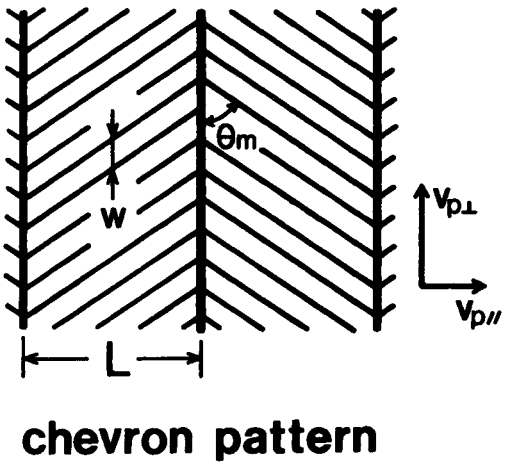

(c)

higher on large-scale straight lines as shown in Fig. 5.1(b). Namely, with increasing ε, this motion becomes more localized. At even higher voltages one has a quasi-periodic structure, where the originally straight lines are alternatingly bended and the areas of different orientations of the stripes are separated by defect streets (Fig. 5.1(c)). Then finally defects become stationary and well ordered. The rolls, however, are inclined with respect to the original WD and propagate, maintaining stationary defect pattern. This herringbone patterns are called chevrons. Thus, the chevron pattern can be said to be periodic defect orientation pattern, because one can regard it as a large number of defect pairs aligned along one-dimension in a regular spatial sequence (see for example Figs. 5.1(d) and (e)). The scale of the chevron pattern is about $d/10$ to $d/20$. By further increasing the field, these periodic defect-orientations produce again a large-scale defect as marked by arrows in Fig. 5.1(d). For a voltage above this, the flow state becomes turbulence. This is a typical hierarchy in the route to turbulence (DSM) in the dielectric regime.

Three parameters characterizing chevron patterns, i.e., inclination angle θ_m, the long wavelength L of defect orientation line and the propagating velocities v_p, are

Downloaded from https://academic.oup.com/ptps/article/doi/10.1143/PTPS.99.458/1882039 by guest on 21 August 2022

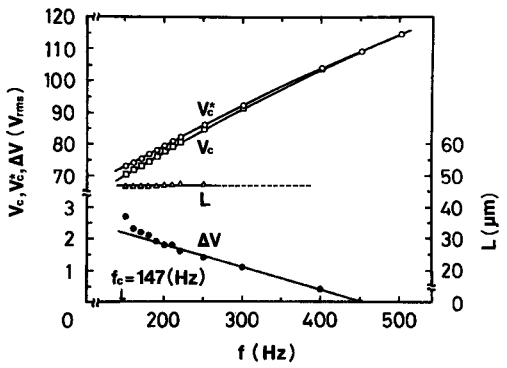

Fig. 5.3. The difference between two bifurcation points as a function of f. V_c and V_c^* are defined from anomalies, e.g., as shown in Fig. 5.2. The sample is different from that in Fig. 5.2.

shown as a function of a voltage in Fig. 5.2 where their definitions are also schematically drawn (Fig. 5.2(c)). At the first bifurcation point V_c=81V, PWD can be observed whose wavelength w is about 5.6 μm with the propagating velocity $v_{p/\!/} \sim 1$ μm/s (Fig. 5.2(a)). The propagating mode in EHD was first observed by the present author (SK) and has been called a propagating WD.[14),17)] This velocity gradually decreases with increase in the voltage and PWD becomes easier to be trapped by defects (Fig. 5.2(b)). On the other hand θ_m increases continuously (roughly linear) from zero at V_c to about 60 degree at V_c^*=89.3V which is defined by the change of the slope of $\theta_m(V)$. Then it almost saturates near 75 degrees at high V. Here V_c^* is the chevron threshold and at this value the defects aline along the defect streets with the wavelength $2L$=160 μm. Here L decreases upto roughly 50% as the voltage increases (Fig. 5.2(a)) and saturates for sufficiently high voltage below DSM point. The typical value of L at V_c^* nearly corresponds to $d/\sqrt{2}$. Above V_c^*, the inclined WD located between two defect lines travels in the direction along the defect line, that is in the direction perpendicular to the original director orientation (rubbing direction). Thus one can define two propagating velocities $v_{p/\!/}$ and $v_{p\perp}$ due to this inclination of rolls, of which voltage dependences are shown in Fig. 5.2(b). As seen in this, the velocity drastically changes at V_c^* showing more than three times faster than that of below. The difference between V_c and V_c^* becomes narrower with increase of an applied frequency as shown in Fig. 5.3. Finally both thresholds come together and no difference can be observed at $f=f_c^*$=450 Hz. This is a kind of co-dimension two bifurcation point

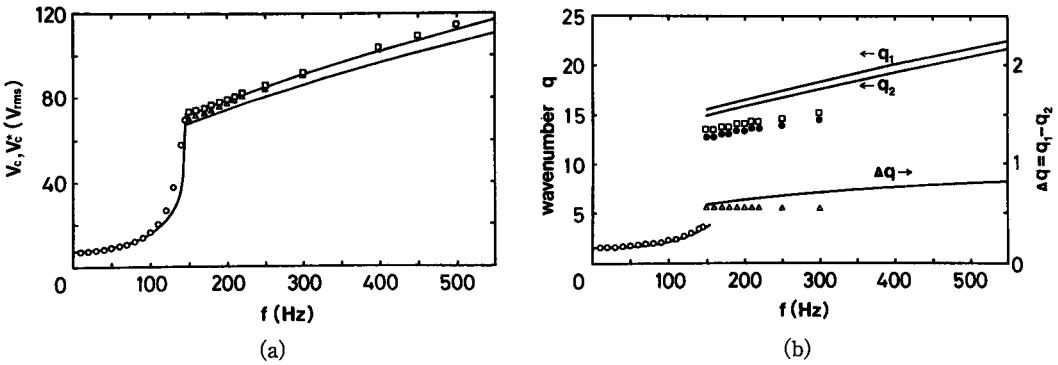

Fig. 5.4. Comparisons between experimental (○, △: V_c; □: V_c^*) and theoretical (solid lines) thresholds (a) both in the conduction and dielectric regimes and experimental plots and theoretical curves (solid lines) for critical wavenumbers (b) as a function of frequency.

Downloaded from https://academic.oup.com/ptps/article/doi/10.1143/PTPS.99.458/1882039 by guest on 21 August 2022

(CDT). Below V_c* the defects move more or less without definite order.

The threshold curve over the whole frequency range (conduction and dielectric regime) is shown in Fig. 5.4(a) and the associated critical wavenumbers at threshold in Fig. 5.4(b). The solid lines in Figs. 5.4(a) and (b) are obtained from the threshold calculation (described in § 2) in the conduction regime and for the two threshold modes in the dielectic regime. In our numerical calculations the material parameters of MBBA at 30 °C have been used. In addition the conductivity-anisotropy was adjusted to $\sigma_{/\!/}/\sigma_{\perp}=1.38$ for approximating the cutoff frequency and the threshold in the dielectric regime as well as the critical wavenumbers (especially for low frequencies). Theoretically we never found the case where both dielectric thresholds cross each other. In Fig. 5.4(b) we also have plotted the wavenumber-difference $\Delta q = q_1 - q_2$ between the two critical modes in the dielecectric regime.

The curves in Fig. 5.4 show the typical behavior that the threshold voltages and the critical wavenumber depend roughly like a square root on the frequency f of the external applied voltage. We show here the thresholds V_c and V_c* in the dielectric regime in an extended frequency range. We find that the chevron threshold comes down to the first threshold at approximately f_c*$\sim 3f_c$. The threshold difference $\Delta V = V_c$*$- V_c$ shows roughly a linear behavior at some distance from f_c and goes to zero at f_c* (see also Fig. 5.3). This decreasing tendency of ΔV is the first measurement, although we reported the existence of a second threshold for the chevron.[17),24)]

The normalized wavenumber of the chevron pattern $2d/2L=50\ \mu$m$/94\ \mu$m~ 0.54 (see Fig. 5.2) is similar to the calculated wavenumber-difference $(q_1-q_2)\sim 0.6$ of both dielectric modes. This similarity gives an indication that the chevrons are the result of the nonlinear interaction of both linear modes, favoring coexistence and this similarity is also the starting point for some qualitative considerations about the origin of the chevrons in the following.

In the case where for both dielectric modes normal rolls have the lowest threshold the superposition of the linear modes has the form,

$$\boldsymbol{U}=A\exp(iq_1x)\boldsymbol{u}_A(z,\omega t)+B\exp(iq_2x)\boldsymbol{u}_B(z,\omega t)+\text{c.c.}\,, \tag{5·1}$$

where q_1 and q_2 are the critical wavenumbers related to the two dielectric modes. The components of $\boldsymbol{u}_i(z,\omega t)$ describe the induced potential, angles of the director and the velocities, as mentioned in § 2. Here q_2 corresponds to the higher threshold and is smaller than q_1 (see Fig. 5.4(b)). A and B are in the simplest case (no defect) complex constants $A=F_1\exp(i\psi_1)$ and $B=F_2\exp(i\psi_2)$, then the linear solution can be brought into the form,

$$\begin{aligned}\boldsymbol{U}=&[2F_1\boldsymbol{u}_A\cos\{((q_1+q_2)x+\psi_1+\psi_2)/2\}\cos\{((q_1-q_2)x+\psi_1-\psi_2)/2\}]\\&+(F_2\boldsymbol{u}_B-F_1\boldsymbol{u}_A)\cos(q_2x+\psi_2)\,.\end{aligned} \tag{5·2}$$

This solution is periodic and displays a beating behavior for finite values of F_1 and F_2.

By assuming a CDT-bifurcation (that means that the threshold difference between two linear instabilities is small) and assuming that both dielectric modes bifurcate supercritically, then the amplitudes would obey the following coupled amplitude equations by symmetry reasons,

Downloaded from https://academic.oup.com/ptps/article/doi/10.1143/PTPS.99.458/1882039 by guest on 21 August 2022

$$\tau_1\partial_t A=\varepsilon A+\xi_1^2\partial_x^2 A-|A|^2A-\gamma_1|B|^2A\,, \tag{5·3a}$$

$$\tau_2\partial_t B=(\varepsilon-D)B+\xi_2^2\partial_x^2 B-|B|^2B-\gamma_2|A|^2B\,. \tag{5·3b}$$

The assumption of a CDT-bifurcation is justified by the small difference of the two thresholds in the dielectric regime, whereas the assumption of the supercritical bifurcation must in principle be proven by a rigorous perturbation calculation starting from the full hydrodynamic equations as demonstrated in Ref. 21). By such a calculation also the coupling coefficients $\gamma_{1,2}$ could be determined. However the experimental observations provide strong evidence that the first and the secondary bifurcations are supercritical, which is some justification of our assumption above. In Eq. (5·3) ε measures the distance from the first threshold and D ($D>0$) measures the difference of the thresholds for both modes. $\xi_{1,2}$, the coherent lengths for both modes are proportional to the curvature of the neutral curve near the minimum. Here they are quite similar and $\tau_{1,2}$ are the relaxation times. The threshold for both modes are in that description $\varepsilon_A=0$ and $\varepsilon_B=D$.

Now we look on constant solutions of Eq. (5·3). There are two single mode solutions $A=F_1$, $B=0$ or $A=0$ and $B=F_2$ with $F_1^2=\varepsilon$ and $F_2^2=\varepsilon-D$. In addition there is a coexisting solution,

$$F_1^2=\lambda_A/(1-\gamma_1\gamma_2) \quad \text{and} \quad F_2^2=\lambda_B/(1-\gamma_1\gamma_2) \tag{5·4}$$

with $\lambda_A=\varepsilon(1-\gamma_1)+D\gamma_1$ and $\lambda_B=\varepsilon(1-\gamma_2)-D$. By a simple stability analysis one can see that the single mode F_1 or F_2 is stable if λ_A or λ_B is negative and for the case $1-\gamma_1\gamma_2>0$ the coexisting solution exists and is stable, when both single modes are unstable. Now depending on the interaction coefficients γ_1 and γ_2 the threshold for coexistence can also be in between the linear threshold $\varepsilon=0$ and $\varepsilon=D$. This is for example the case for γ_1, $\gamma_2<0$ and $1-\gamma_1\gamma_2>0$. Choosing e.g., $\|\gamma_2\|\ll 1$ and let decrease $\gamma_2<0$ more and more, the threshold for coexistence then comes down to that of the mode A. When one wants to make the analogy between the threshold for the chevrons then $\gamma_2<0$ must decrease with frequency to explain the observation in Fig. 5.4(a). This shows the possibility that chevrons can have as the origin the interaction of both linear modes.

Now the following picture for the formation of the chevrons is imaginable. Immediately above the first threshold defects are created by the mechanism which is perhaps similar to that which induces also the defects in FWD. By increasing the voltage the coexistence becomes possible and due to the beating of the solution in Eq. (5·2) the defects order along the lines where the envelope has the smallest value. The reason for this ordering of the defects would be, that in the defect core the amplitude tends to zero therefore the undistorted amplitude must be less reduced in a region where the defectless state has a smaller amplitude than in the areas with a larger amplitude. This effect is especially important when the beating wavelength is larger than the length over which the amplitude in the defect core is varying. Otherwise the pinning of the defect with respect to such an argument can be neglected.

In accordance with our observation,[16),17),28)] as further details, the chevron pattern is a skin convection near electrodes. The director oscillation following the frequency

Downloaded from https://academic.oup.com/ptps/article/doi/10.1143/PTPS.99.458/1882039 by guest on 21 August 2022

of an applied field is observed in the bulk of a cell.[58] In this situation, the bulk oscillation could influence the macroscopic convection as a background disturbance. This is probably important and must be taken into account as well as a flexoelectric effect. Such quite different temporal scales (characteristic times; the order of second for the convection near surface and milisecond for an oscillation of the director in the bulk) and spatial scale may be an origin for a Hopf-bifurcation.

The important fact observed in defect motions for both conductive and dielectric regimes is following. If gliding motion is more actively oscillatory and widely happens, the temporal order like oscillatory patterns (PWD, chevrons and oscillatory grid pattern (GP)) will be more favourably formed via new bifurcation when increasing a voltage. In contrast to this if it is inactive the stationary patterns like perfect GP[16),17),23)] will be observed. Thus defect motions indicate in some sense the characteristics of newly appearing patterns through further bifurcation.

§ 6. Magnetic field effects for EHD

The threshold V_c for the onset of EHD and the nonlinear stable-wave-number strongly depend on a magnetic field H as already reported in detail.[19)] On the magnetic field effects there are two physically quite different directions of a magnetic field against an electric field E, i.e., $H \perp E$ and $H /\!/ E$ (namely H is applied in the z-direction: H_z).[19),60)] We indicate simply H (i.e. H_x and H_y) for the former case and $H_{/\!/}$ for the latter and here mainly study for $H_\perp$. $H_\perp$ is rotated in the plane parallel to the

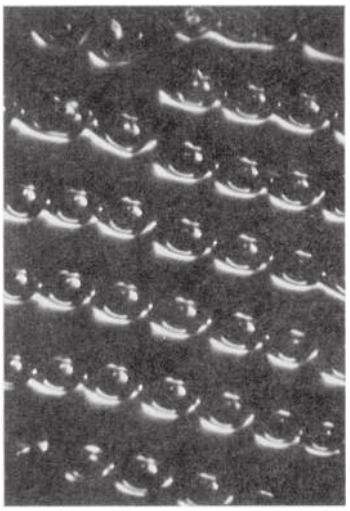

Fig. 6.1. Pattern of homeotropically changed orientation by $H_{/\!/}$=3900 Oe in EHD (V=20V and f=50 Hz).

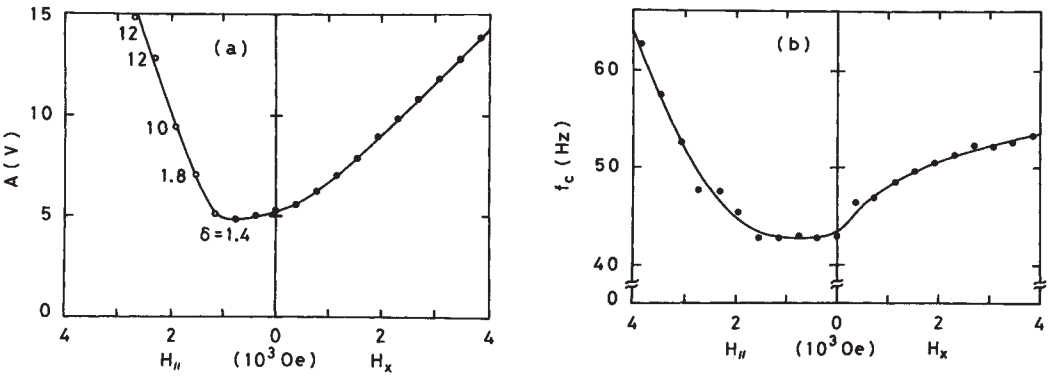

Fig. 6.2. Normalized threshold voltage $A(= V_c(1-(f/f_c)^\delta))$ and f_c as a function of intensity of magnetic field for two different directions.

Downloaded from https://academic.oup.com/ptps/article/doi/10.1143/PTPS.99.458/1882039 by guest on 21 August 2022

electrodes.[19),60)] Then again different situations can be realized, i.e., applying H_x perpendicular to the roll axis (parallel to the director) and H_y parallel to the roll axis. H_x stabilizes the director orientation but H_y induces Freedericksz transition in a planar orientation which leads to inclination of a roll for $H>H_c$ and even make it perpendicular to the original direction for a sufficiently high intensity. Here H_c is a critical field for the onset of Freedericksz transition. On the other hand, $H_{//}$ can lead homeotropic orientation by the Freedericksz transition above a certain threshold value H_{th} different from H_c, and typical patterns due to the transition to homeotropic orientation are shown in Fig. 6.1.

Figure 6.2 shows H-dependences of V_c and f_c for two different H-directions, H_x and $H_{//}$ (i.e., H_z). Here A is a normalized threshold voltage obtained from the best fit due to the equation,

$$V_c=A/(1-(f/f_c)^{\delta}), \tag{6·1}$$

where $\delta=1$ for closed circles (●: mainly for H_x) and $\delta>1$ ranging from 1.4 to 12 for open circles (○: for $H_{//}$). For the region of H-value indicated by closed circles, ordinary WD was seen at thresholds. But for the region of open circles the pattern shown in Fig. 6.1 was observed, where no WD appeared even by increase of voltage and the route to DSM was completely different. For $H_{//}$, thus, both thresholds V_c and f_c increase very steeply as the strength of H increases. This indicates that $H_{//}$ induces a homeotropic orientation by which EHD can be suppressed. In contrast, the dependence of both V_c and f_c on the intensity of H_x is not strong. A and f_c are proportional to H_x and to $H_x^{1/2}$ respectively. These are due to competition between the stabilizing effect of H_x and the destabilizing effect due to the EHD instability. The frequency dependence of V_c is shown in Fig. 6.3 for $H_x=1000$ Oe and $H_{//}=3900$ Oe. The large difference between them can be seen. For H_x, the smooth change of

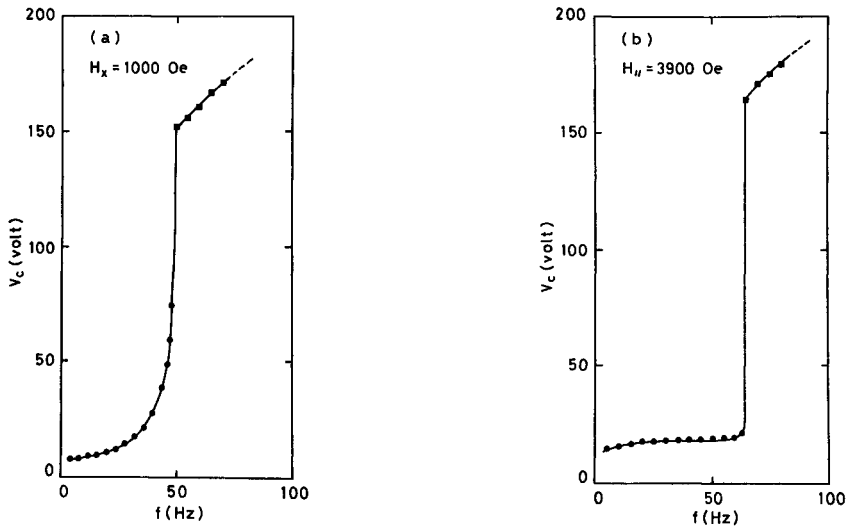

Fig. 6.3. Frequency dependence of threshold voltage V_c of WD for two different magnetic fields H_x =1000 Oe (a) and $H_{//}$=3900 Oe (b).

Downloaded from https://academic.oup.com/ptps/article/doi/10.1143/PTPS.99.458/1882039 by guest on 21 August 2022

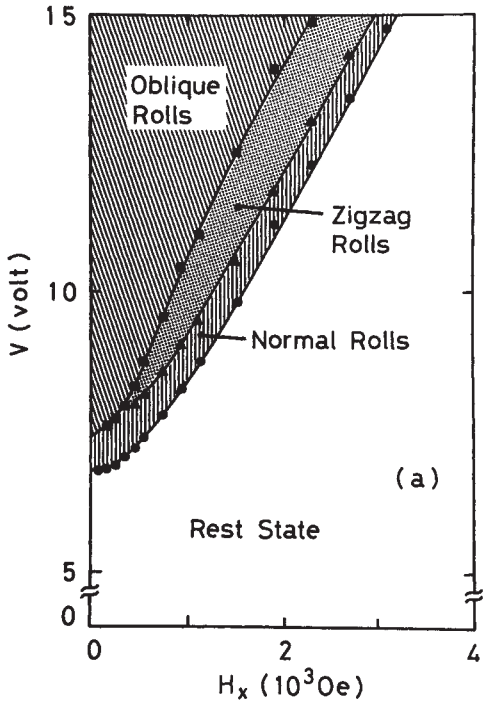

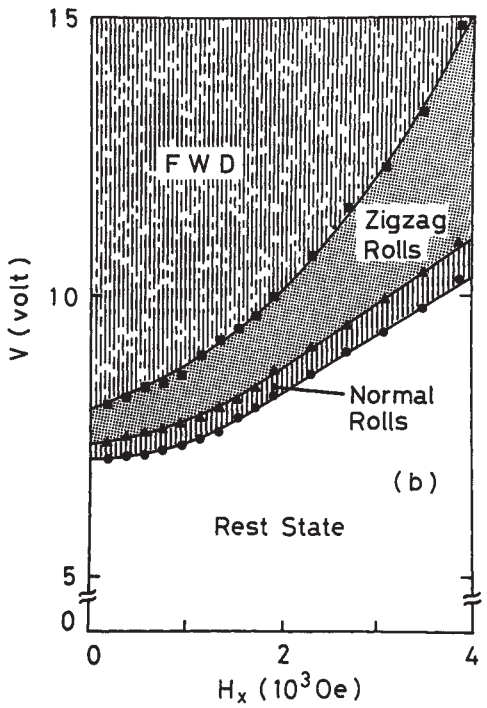

Fig. 6.4. Pattern diagram relatively near threshold. (a) $d=100$ μm, $\Gamma_{/\!/}=14$, $\Gamma_{\perp}=10$ (b) $d=50$ μm, $\Gamma_{/\!/}=\Gamma_{\perp}=120$.

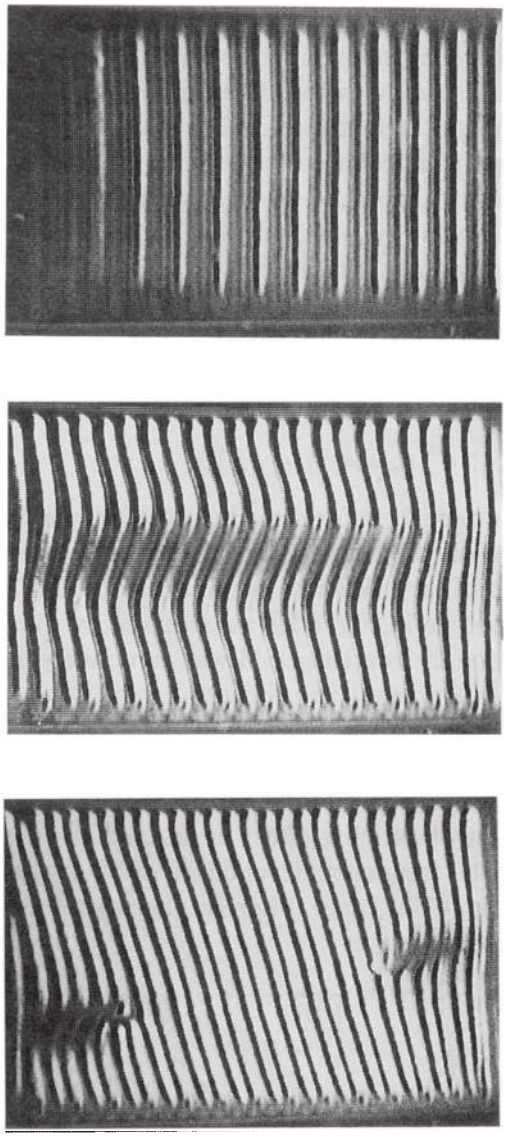

Fig. 6.5. Photographs from normal to oblique rolls in Fig. 6.4(a).
$H_x=970$ Oe, $V=8.1$ to 10.4 V. (from the up to the bottom pictures)

Downloaded from https://academic.oup.com/ptps/article/doi/10.1143/PTPS.99.458/1882039 by guest on 21 August 2022

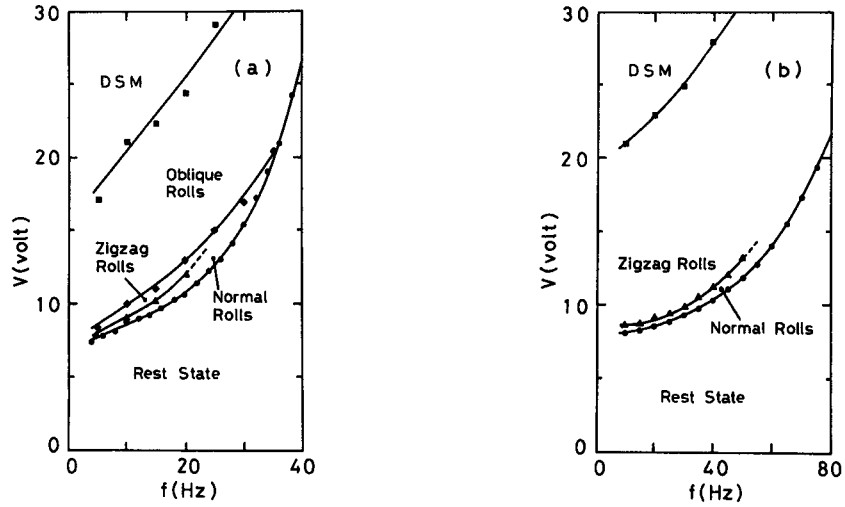

Fig. 6.6. Pattern diagram under magnetic field $H=1000$ Oe (a) for $d=100$ μm and $\Gamma=14\times10$, and 2000 Oe (b) for $d=50$ μm and $\Gamma=120\times120$.

V_c is observed but for $H_{//}$ it is discrete and shows a jump with very large gap to the dielectric regime. For $f<f_c$, V_c is almost constant with relatively large threshold about 15-20V for $H_{//}$, which is twice to three times larger than a common value for H_x. For both cases however the chevron pattern is observed in the dielectric regime.

Figure 6.4 shows the typical phase diagram of patterns as a function of H_x in relatively small V for two different thickness $d=100$ μm (a) and 50 μm (b) at fixed frequency. Both are quite different and the reason is unknown at this moment. Typical change of patterns from normal to oblique rolls is given in Fig. 6.5. Figure 6.6 on the other hand shows the phase diagram of patterns as a function of frequency under fixed H_x (=1000 Oe (a) and 2000 Oe (b)) in the conduction regime ($f<f_c$). Lifshitz point can be observed at $f\sim36$ Hz in Fig. 6.6(a), which will be described in anisotropic fluids like NLCs by the equation,[20)~22),61)]

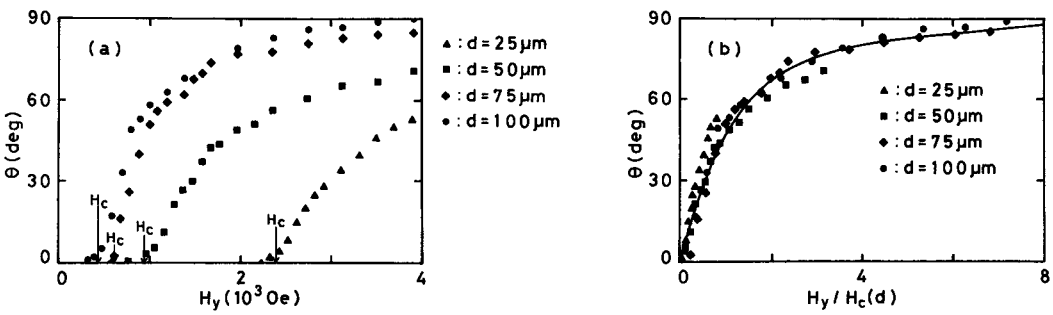

Fig. 6.7. Inclination angle of rolls to original direction as a function of a magnetic field H_y for samples with various thickness d. H_c is the critical field for the Freedericksz transition. The universal curve proportional to $\tan^{-1}(H/H_c-1)$[19] can be observed independently of d in (b). (a) raw data (b) normalized data by each H_c.

Downloaded from https://academic.oup.com/ptps/article/doi/10.1143/PTPS.99.458/1882039 by guest on 21 August 2022

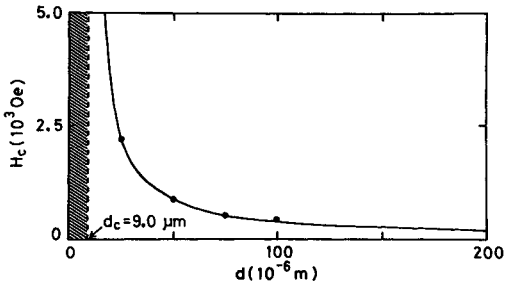

Fig. 6.8. Threshold magnetic field H_c as a function of d. The solid line due to $H_c=a/(d-d_c)$ with a=3.53 Oe·m.

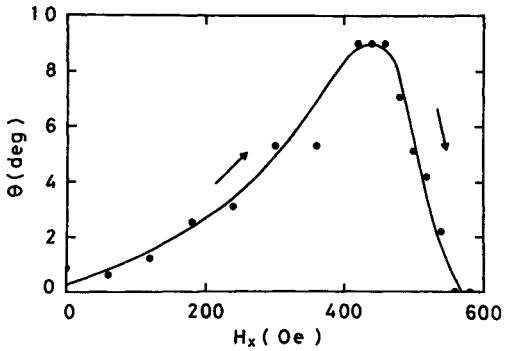

Fig. 6.9. Inclination angle θ as a function of H_x. This data is measured along H_x-axis at fixed V =7.4V ($\varepsilon(H_x=0)=0.18$) in Fig. 6.4(a).

$$\partial_t A=A+[\partial_x{}^2-ik_1\partial_x\partial_y{}^2+k_2\partial_y{}^2-\partial_y{}^4]A-|A|^2A\,, \tag{6·2}$$

containing the magnetic field effect. Here $k_1=2$ and $k_2=0$ for R-B convection in isotropic fluids. Details will be elsewhere.[29]

The magnetic field effect is closely related to the competition among surface anchoring, elastic and magnetic forces. The surface anchoring force penetrates into the bulk and therefore the H-response of bulk depends on sample thickness d. The bulk in a sample with small d is more influenced from glass surfaces by anchoring force. Such a behavior is tested for various d and shown in Fig. 6.7. In this figure, the inclination angle θ of a roll axis to the original direction is plotted as a function of H_y at the threshold; $\varepsilon(H_y)=0$. A roll starts to incline from the threshold H_c which increases with decrease of d. Such a behavior is given by the relation,

$$H_c=a/(d-d_c) \tag{6·3}$$

as shown in Fig. 6.8 by the solid line. Here $d_c=9$ μm, $a=3.53$ Oe·m and $H_{c0}\sim 390$ Oe ($=a/d_c$). Physically, d_c corresponds to the thickness of the surface layer.

The inclination angle θ of a zig-zag roll changes with a strength of H_x. The dependence of θ on H_x is shown in Fig. 6.9. For $H_x=0$, the roll has a small θ. Increasing H_x, θ increases. After it shows the maximum value $\theta=9$ degrees at 440 Oe, θ sharply decreases with increase of H_x. This behavior is understandable from the phase diagram shown in Fig. 6.4(a). Namely, it is probably due to the neighborhood of Lifshitz point. Other magnetic field effects have been already discussed in detail.[19]

§ 7. Summary

FWD is a kind of weak turbulence and shows nonperiodic feature in time and in space. We showed spatio-temporally nonperiodic motions of defects in § 3. We called this the defect chaos (topological chaos). Coullet et al. tried to understand such complicated motions in isotropic systems numerically by use of complex TDGL equations.[10),11] The description on defect turbulence by these model equations was

Downloaded from https://academic.oup.com/ptps/article/doi/10.1143/PTPS.99.458/1882039 by guest on 21 August 2022

not yet fully successful and the bifurcation mechanism to FWD is still unknown. In R-B case it is considered that nucleation and annihilation of defects will be due to a mean flow. In EHD however both long-range space change interaction and elastic interaction seem to be more important from the fact that the transient motions of a single defect show oscillatory tendency of climbing and gliding velocities in WD, which has never been observed in shear flow of NLCs. These two interactions therefore must be explicitly taken into account in full amplitude equations. Then properties of bifurcation to FWD may be discussed. It is also worth noting that the state with more oscillatory defect motions changes into one with a temporal order after next bifurcation. In the case of less oscillatory motions, it changes rather into the stationary state after next bifurcation. Thus the precise investigation for motion of a single defect is very important.[19),62),63)]

We are interested in the shape of an attractor for nonperiodic motion of defects in FWD and in its dimensionality with respect to model constructions. We tried to obtain the correlation dimension of the nonperiodic defect motions but did not well succeed. We have still an open question about types of intermittency in FWD. It might be a new type different from three types already observed.[64)] In FWD $1/f$ type power spectrum has been observed due to intermittent change of the number of defects with temporal nonperiodicity.[11)] $1/f$ spectrum for resistance fluctuations associated with defect interactions in metalic nanoconstrictions has recently been reported.[65)] The similarity between its origin of $1/f$ noise and one in the present system is very interesting and might be universal in a sense of a connection with defect motions.

We have also reported in detail the transition kinetics between the turbulent states DSM1 and DSM2. We found that the transition is local. This local transition also shares similarities with classical nucleation phenomena, however there is an essential difference in the growth process of the nuclei: Its velocity cannot be reversed. It has been revealed that, during the transition to the DSM2-state, disclinations are created——presumably by eddies in the velocity field which are already present in the DSM1 state. In a sense the DSM2 state can be called as "disclination turbulence". In that respect the DSM1-DSM2 transition has a great similarity to the transition between the two turbulent states in superfluid HeII, where one has a change in the vortex filament density. We have demonstrated in the present article the analogy between disclination in EHD and vortex-filament in superfluid turbulence of HeII. It is very difficult to check whether this transition in HeII however is spatially homogeneous (homogeneous bifurcation) or starts from nucleation like the present case because of difficulty of direct visualization. In this sense, EHD has a great advantage for studying such topological instabilities.

The dynamic behavior of the chevron is strongly related to the defect motions which become more active and widely moving with oscillatory tendency in space as f is approached to f_c. We showed that the chevron pattern was formed by the periodic defect orientation via a second bifurcation point. The propagating velocity and width of the defect orientation were considerably changed via that point. We also found co-dimension-two bifurcation point at f_c^* where the first and the second bifurcations occurred at the same threshold. There is no quantitative theoretical work in this region, except linear theory done by Bayreuth group.[20)~22),35)] Most will

Downloaded from https://academic.oup.com/ptps/article/doi/10.1143/PTPS.99.458/1882039 by guest on 21 August 2022

be in the future study.

In magnetic field effects, we mainly discussed on the static aspects. The characteristic changes of V_c and f_c were shown for both of which strongly depend on the strength of a magnetic field. The Freedericksz transition in convective state was observed. The thickness dependence of H_c was described and evaluated. The magnetic-field-induced Lifshitz point was also observed. Theoretical works on this will be in the future.

We have presented many new aspects observed in EHD in this article most of which should be understood more precisely. We could explain some of threshold effects theoretically. However it is not fully satisfactory yet. We hope that our work will give valuable hints for the future theoretical works in particular on highly nonlinear aspects, e.g., on nucleation and annihilation of defects, their motions, defect chaos, turbulent-domain nucleation, and its front propagation.

Acknowledgements

It is a pleasure to thank M. Andoh, M. Kohno, N. Chizumi and W. Thom for fruitful interaction and F. H. Busse, K. Kawasaki, L. Kramer and I. Rehberg for helpful discussions. This work is in part supported by the Grant in Aid for Scientific Research from the Ministry of Education, Culture and Science in Japan (No. 01540302) and from the Deutsche Forschungsgemeinschaft through SFB 213 (Topomak). One of us (WZ) acknowledges also the visiting scholarship of the Kyushu Institute of Technology.

References

1) C. Normand, Y. Pomeau and M. G. Velarde, Rev. Mod. Phys. **49** (1977), 581.
2) J. P. Gollub and S. V. Benson, J. Fluid Mech. **100** (1980), 449.
3) V. Steinberg, G. Ahlers and D. S. Cannell, Physica Scripta **32** (1985), 534.
4) H. L. Swinney and J. P. Gollub (ed.), *Hydrodynamic Instabilities and the Transition to Turbulence 2nd ed.* (Springer, Berlin, 1986).
5) R. Williams, J. Chem. Phys. **39** (1963), 384.
6) P. G. de Gennes, *The Physics of Liquid Crystals 3rd ed.* (Oxford, Clarendon, 1982).
L. M. Blinov, *Electro-Optical and Magneto-Optical Properties of Liquid Crystals* (Wiley, New York, 1983).
7) J. Fineberg, E. Moses and V. Steinberg, Phys. Rev. Lett. **61** (1988), 838.
P. Kolodner and C. M. Surko, ibid. 842.
L. Lam and H. C. Morris, *Wave Phenomena* (Springer, New York, 1989).
8) O. Lhost and J. K. Platten, Phys. Rev. **A38** (1988), 3147.
9) S. Kai and K. Hirakawa, Memoirs Fac. Engin. Kyushu Univ. **36** (1977), 269.
I. Rehberg, S. Rasenat, J. Fineberg, M. de la Torre Juarez and V. Steinberg, Phys. Rev. Lett. **61** (1988), 2449.
A. Joet and R. Ribbota, Phys. Rev. Lett. **60** (1988), 2164.
R. Ribbota, A. Joet and L. Lei, Phys. Rev. Lett. **56** (1986), 1595.
10) P. Coullet, C. Elphick, L. Gil and J. Lega, Phys. Rev. Lett. **59** (1987), 884.
11) P. Coullet, L. Gil and J. Lega, Phys. Rev. Lett. **62** (1989), 1619.
12) S. Kai, N. Chizumi and M. Kohno, J. Phys. Soc. Jpn. **58** (1989), 1493.
13) G. K. Batchelor, *The Theory of Homogeneous Turbulence* (The University Press, Cambridge, 1953).
A. C. Monin and A. M. Yaglom, *Statistical Hydrodynamics* (MIT Press, Boston, 1970), vol. 1.
14) S. Kai and K. Hirakawa, Prog. Theor. Phys. Suppl. No. 64 (1978), 212.

Downloaded from https://academic.oup.com/ptps/article/doi/10.1143/PTPS.99.458/1882039 by guest on 21 August 2022

15) S. Kai, *Noise in Nonlinear Dynamical Systems,* ed. F. Moss and P. V. E. McClintock (Cambridge University Press, Cambridge, 1989), vol. 3, chap. 2.
S. Kai, N. Chizumi and M. Kohno, J. Phys. Soc. Jpn. **58** (1989), 3541.
16) S. Kai, K. Yamaguchi and K. Hirakawa, Jpn. J. Appl. Phys. **14** (1975), 1653.
17) K. Hirakawa and S. Kai, Mol. Cryst. Liq. Cryst. **40** (1977), 261.
18) A. Joets and R. Ribotta, J. de Phys. **47** (1986), 1595.
19) S. Kai, M. Kohno and N. Chizumi, Phys. Rev. **A40** (1989), 6554.
20) W. Zimmermann and L. Kramer, Phys. Rev. Lett. **55** (1985), 402.
21) E. Bodenshatz, W. Zimmermann and L. Kramer, J. de Phys. **49** (1988), 1875.
22) W. Thom, W. Zimmermann and L. Kramer, Liquid Crystals **5** (1989), 699.
23) S. Kai and K. Hirakawa, Solid State Commun. **18** (1976), 1573.
S. Kai, M. Araoka, H. Yamazaki and K. Hirakawa, J. Phys. Soc. Jpn. **46** (1979), 393, 401.
24) S. Kai and K. Hirakawa, Solid State Commun. **18** (1976), 1579.
25) J. T. Tough, *Superfluid Turbulence in Low Temperature Physics,* ed. D. F. Brewer (North-Holland, Amsterdam, 1982), vol. 8, p. 134.
26) D. Griswold and J. T. Tough, Phys. Rev. **A36** (1987), 1360.
27) J. T. Tough, *Noise in Nonlinear Dynamical Systems,* ed. F. Moss and P. V. E. McClintock (Cambridge Univ. Press, Cambridge, 1989), vol. 3, chap. 1 and literature cited therein.
28) H. Yamazaki, S. Kai and K. Hirakawa, J. Phys. Soc. Jpn. **56** (1987), 502.
29) S. Kai, M. Kohno, M. Andoh and W. Zimmermann, in preparation.
30) S. Kai, W. Zimmermann, M. Kohno and M. Andoh, in preparation.
31) W. Helfrich, J. Chem. Phys. **51** (1969), 4092.
32) E. Dubois-Violette, P. G. de Gennes and O. Parodi, J. de Phys. **32** (1971), 305.
33) C. Hilsum and F. C. Saunders, Mol. Cryst. Liq. Cryst. **64** (1980), 25.
34) N. V. Madhusudana and V. A. Raghunathan, Mol. Cryst. Liq. Cryst. Lett. **5** (1988), 201.
35) W. Zimmermann and W. Thom, J. de Phys. to be published.
36) L. Cesari, *Asymtotic Behavior and Stability Problems in Ordinary Differential Equations* (Springer, Berlin, 1971).
37) M. R. E. Proctor and C. A. Jones, J. Fluid. Mech. **188** (1988), 301.
38) H. W. de Jeu and J. van der Veen, Phys. Lett. **A44** (1973), 277.
39) H. R. Brand, S. Kai and S. Wakabayashi, Phys. Rev. Lett. **54** (1985), 255.
S. Kai, H. Fukunaga and H. R. Brand, J. Phys. Soc. Jpn. **56** (1987), 3759.
40) H. Yamazaki, S. Kai and K. Hirakawa, Memoirs Fac. Engin. Kyushu Univ. **44** (1984), 317.
41) H. Yamazaki, K. Hirakawa and S. Kai, Mol. Cryst. Liq. Cryst. **122** (1985), 41.
42) P. Grassberger and I. Procaccia, Phys. Rev. Lett. **50** (1983), 153; Physica **9D** (1983), 189.
43) S. Kai, N. Yositsune and K. Hirakawa, J. Phys. Soc. Jpn. **40** (1976), 267.
44) A. Sussman, Appl. Phys. Lett. **21** (1972), 269.
45) R. Chang, J. Appl. Phys. **44** (1973), 1885.
46) P. M. Alt and M. J. Freiser, J. Appl. Phys. **45** (1974), 3237.
47) T. Krupkowski and W. Ruszkiewicz, Mol. Cryst. Liq. Cryst. **49** (1978), 47.
48) S. Kai, W. Zimmermann, M. Andoh and N. Chizumi, J. Phys. Soc. Jpn. **58** (1989), 3449; Phys. Rev. Lett. **64** (1990), 1111.
49) H. Orihara and Y. Ishibashi, Jpn. J. Appl. Phys. **23** (1984), 1274.
S. Kai, Y. Kunitake and M. Imasaki, Ferroelectrics **85** (1988), 521.
50) F. F. Abraham, *Homogeneous Nucleation Theory* (Academic Press, New York, 1974).
51) E. Ben-Jacob, H. R. Brand, G. Dee, L. Kramer and J. S. Langer, Physica **D14** (1985), 348.
W. Saarloos, Preprint (1989).
52) M. F. Schumaker and W. Horsthemke, Phys. Rev. **A36** (1987), 354.
53) M. Gad-El-Hak, R. F. Blackwelder and J. J. Riley, J. Fluid Mech. **110** (1981), 73.
D. R. Carlson, S. E. Widnall and M. F. Peeters, J. Fluid Mech. **121** (1982), 487.
54) F. Heslot, B. Castaing and A. Libchaber, Phys. Rev. **A36** (1987), 5870.
55) S. Kai, M. Araoka, H. Yamazaki and K. Hirakawa, J. Phys. Soc. Jpn. **46** (1979), 393.
S. Kai, M. Andoh and W. Zimmermann, Mod. Phys. Lett. **B** (to appear).

Downloaded from https://academic.oup.com/ptps/article/doi/10.1143/PTPS.99.458/1882039 by guest on 21 August 2022

56) S. Kai, T. Kai and K. Hirakawa, J. Phys. Soc. Jpn. **46** (1979), 699.
57) S. Kai, H. Fukunaga and H. R. Brand, J. Stat. Phys. **54** (1989), 1133.
58) S. Kai, S. Wakabayashi and M. Imasaki, Phys. Rev. **A33** (1986), 2612.
59) V. A. Raghunathan and N. V. Madhusudana, J. Phys. (India) **31** (1988), L163.
60) I. Teucher and M. M. Labes, J. Chem. Phys. **54** (1971), 4130.
61) W. Pesch and L. Kramer, Z. Phys. **B63** (1986), 121.
62) H. Yamazaki, S. Kai and K. Hirakawa, J. Phys. Soc. Jpn. **56** (1987), 1.
63) S. Nasuno and Y. Sawada, Phys. Rev. **A40** (1989), 3457.
64) Y. Pomeau and P. Manneville, Commun. Math. Phys. **19** (1980), 74.
65) K. S. Ralls and R. A. Buhrman, Phys. Rev. Lett. **60** (1988), 2434.

Downloaded from https://academic.oup.com/ptps/article/doi/10.1143/PTPS.99.458/1882039 by guest on 21 August 2022